



Unraveling the real active site of reaction-induced trivalent vanadium ion in VO_x/Al₂O₃ catalysts for boosting photothermal catalytic propane non-oxidative dehydrogenation

Bohan Feng^{a,1}, Dong Li^{a,c,1}, Jing Xiong^a, Yuechang Wei^{a,b,*}, Yuanfeng Li^{a,b,c}, Zhen Zhao^{a,c}, Weiyu Song^a, Xiangyang Ji^a, Jian Liu^a, Chunming Xu^{a,**}

^a State Key Laboratory of Heavy Oil Processing, College of Science, China University of Petroleum, Beijing 102249, China

^b Key Laboratory of Optical Detection Technology for Oil and Gas, China University of Petroleum, Beijing 102249, China

^c Institute of Catalysis for Energy and Environment, Shenyang Normal University, Shenyang 110034, China

ARTICLE INFO

Keywords:

Propane non-oxidative dehydrogenation
Vanadium oxide
Low temperature
Photothermal catalysis
Solar utilization

ABSTRACT

Herein, nano-catalysts of vanadium oxides (VO_x) deposited on Al₂O₃ support were synthesized by the impregnation method. The VO_x/Al₂O₃ catalysts show super-catalytic performances during photothermal propane non-oxidative dehydrogenation (PDH) reaction, and their catalytic performances are strongly dependent on the surface states of supported VO_x. The propane conversion of VO_x/Al₂O₃-25 catalyst is 20.7 % at 480 °C under irradiation, and its relative deactivated rate is 0.018 in 12 h. Based on in-situ structure characterizations, the V₂O₅ on the surface of the support is transformed into the mono-layer dispersed VO_x during the photothermal PDH, which can further be reconstructed into highly dispersed V₂O₃ nanocrystals induced by the reaction conditions. Combined with the results of experiments and theoretical calculations, the role of in-situ formed V₂O₃ is revealed: the unique 3D structure of V³⁺ ions can induce the localized surface plasmon resonance effect and strengthen visible light adsorption, which promotes C-H breaking in C₃H₈ molecules.

1. Introduction

Propylene (C₃H₆) is an extremely vital hydrocarbon compound, which is employed as an intermediate of a vast array of chemicals, including polypropylene, propylene oxide, propylene alcohol, etc [1–3]. Generally, the product of propylene in international markets is mainly provided by the cracking industry of naphtha. However, the change in cracking processes resulted in a propylene shortage [4]. The propane (C₃H₈) non-oxidative dehydrogenation (PDH) technology can realize the selective and effective propane conversion into propylene, which provides a promising way to satisfy the future demand for propylene [5]. And the exploration of shale gas provides low-cost feedstocks for PDH. However, the non-polar C-H bonds in propane have a stable chemical state with a high bond energy [6,7]. To obtain the desired propylene yield, a high temperature of about 650 °C is needed to meet the strong endothermic reaction for C-H bond cleavage. During the actual industrial process of PDH, the high reaction temperature usually led to

high-energy consumption, severe coke deposition, and structural collapse of the catalysts [8–10]. Thus, it is urgently required to renovate the traditional PDH technology.

Recently, the novel photothermal catalysis technology, which can decrease the apparent reaction temperature by utilizing alternative and abundant light energy, exhibits the conspicuous advantage of saving on non-renewable fossil fuels [11]. The mechanism of photothermal catalysis is to convert absorbed photons to heat via the excitation and relaxation of the photo-induced electron [12]. In addition, the heating site could be accurately controlled in photothermal active sites, which prevents extra energy loss [13]. Several catalytic materials have been found to exhibit photothermal performances, and are feasible to prompt industrially essential reactions, such as metal, metal alloy, metal oxide, non-metallic materials, etc [14]. Within this context, it is a promising path to rationally designing photothermal co-catalytic PDH technologies [15,16]. However, the oxygen-free PDH co-worked by solar light is still rarely reported. Thus, an in-depth understanding of the nature of active

* Corresponding author at: State Key Laboratory of Heavy Oil Processing, College of Science, China University of Petroleum, Beijing 102249, China.

** Corresponding author.

E-mail addresses: weiyu@cup.edu.cn (Y. Wei), xcm@cup.edu.cn (C. Xu).

¹ These authors contributed equally.

sites and the reaction mechanism during photothermal PDH reaction is the potential to solve the technical bottleneck of single thermal catalytic PDH.

Supported vanadium oxide (VO_x) is a kind of effective catalyst for PDH, which exhibited high activity, selectivity, and regeneration stability. In addition, the supported VO_x catalysts have been widely recognized as possessing excellent light absorption, exhibiting the possibility of harvesting solar light energy to drive dehydrogenation. The chemical state and light adsorption behavior of VO_x is highly dependent on its morphology, which is determined by the principle of spontaneous monolayer dispersion [17]. At a low surface concentration of VO_x species, supported VO_x species mainly present as an isolated VO_x state. The VO_x microstructure can polymerize with others through V-O-V bonds with increasing VO_x loading amounts. The polymeric VO_x spontaneously disperses on the carrier in a 2-dimensional (2D) surface mono-layer [18]. The surface concentration of VO_x species is higher than the mono-layer dispersion threshold, which can result in the growing epitaxially of 2D VO_x mono-layer and the formation of 3-dimensional (3D) VO_x species. The 3D structure reduces the number of exposed active sites of VO_x species. In addition, the coupling effect in 3D VO_x species decreases the barrier of structure-sensitive side reactions [19]. Thus, the isolated and polymeric VO_x possessed higher PDH activity and stability than the 3D VO_x species. Until now, the studies on supported VO_x catalysts mainly contribute to designing mono-layer dispersed vanadyl active sites for PDH. However, the performance of these catalysts could not satisfy the desired yield in industrial [20–23]. It is still a challenge to obtain a novel strategy for breaking the activity limitation of the mono-layer VO_x catalysts.

Herein, a series of $\text{VO}_x/\text{Al}_2\text{O}_3$ model catalysts were prepared by the impregnation method. Their VO_x surface state, including isolated VO_x , polymeric VO_x , and V_2O_5 , is controlled by varying VO_x loading amounts. Under UV and visible (VIS) light irradiation, the propane conversion of $\text{VO}_x/\text{Al}_2\text{O}_3$ catalyst could be significantly promoted by the photothermal synergy effect. Surprisingly, the V_2O_5 -abundant catalysts, which had poor catalytic performance in traditional thermal catalysis, exhibited much better catalytic performance for photothermal PDH than mono-dispersed catalysts. Based on the results of in-situ XRD and Raman spectra, it is found that the surface-active sites of $\text{VO}_x/\text{Al}_2\text{O}_3$ catalysts have occurred the reconstruction, and supported V_2O_5 species can transform into 2D polymeric VO_x and even highly dispersed 3D V_2O_3 induced by propane molecule. Compared with 2D polymeric VO_x , the unique 3D structure of V_2O_3 can improve the d-d transition and the localized surface plasmon resonance (LSPR) effect, which broadens its optical absorption capacity for the visible light region. Thus, V_2O_5 -abundant catalysts show improved catalytic performance during photothermal PDH in comparison with the isolated and polymeric VO_x .

2. Experiment methods

2.1. Catalyst preparations

All chemicals were obtained from Shanghai Macklin Biochemical Co., Ltd. Al_2O_3 supports were obtained by calcining pseudo-boehmite in a muffle furnace at 600 °C for 4 h. Al_2O_3 was used as the carrier because of its chemical inertness and photo-insensitivity. $\text{VO}_x/\text{Al}_2\text{O}_3$ catalysts were synthesized by the impregnation method using NH_4VO_3 and oxalic acid solution, named $\text{VO}_x/\text{Al}_2\text{O}_3$ -n, where n wt % is the mass weight percent of V atoms, and its values are 1, 5, 10, 15, 25 and 50 wt %. After the impregnation, the samples were dried at 80 °C overnight and then calcined at 500 °C for 4 h. Bulk V_2O_5 catalyst was obtained by calcining NH_4VO_3 at 500 °C for 4 h.

2.2. Catalyst characterizations

The X-ray diffraction (XRD) patterns in the range of 5–90° were obtained by a Bruker D8 Advance diffractometer using $\text{Cu K}\alpha$ ($\lambda =$

0.15406 nm). The particle size of V_2O_5 and V_2O_3 was calculated according to the intensity of characteristic peaks of (110) and (104) facets, respectively. The quantitative equation was listed as follows Eq. (1).

$$P_s = K\lambda/\beta\cos\theta \quad (1)$$

K is the Scherrer constant. λ is the wavelength of X-ray sources. β is the full width at half maxima (FWHM). θ is the peak position.

N_2 adsorption-desorption isotherms at –196 °C were recorded using a Micromeritics ASAP-2010 porosimetry analyzer. Before the tests, all the samples were pretreated at 300 °C for 2 h. The Brunauer–Emmett–Teller (BET) method were used to calculate the specific surface areas, total pore volumes, and average pore sizes of the $\text{VO}_x/\text{Al}_2\text{O}_3$ catalysts. Ex-situ Raman spectra were obtained by an Horiba HR Evolution spectrometer in the range of 200–1400 cm^{-1} with an excitation wavelength of 325 and 532 nm, respectively. High-angle annular dark-field scanning transmission electron microscope (HAADF-STEM) and corresponding element mapping were obtained by a Talos F200X equipment. Ultraviolet-Visible-Near-infrared (UV–VIS–NIR) spectra were measured on a SHIMADZU UV-3600i plus spectrophotometer with a diffuse reflectance spectroscopy (DRS) technique in the range of 200–2600 nm, and BaSO_4 was used as standards. The E_g values were obtained by the intersection point of the vertical and horizontal parts of obtained spectra calculated by the Kubelka–Munk function [24]. Vanadium compounds with known V-O-V bond numbers were used as an internal standard to describe the coordination structure of $\text{VO}_x/\text{Al}_2\text{O}_3$ catalysts.

The hydrogen temperature-programmed reduction (H_2 -TPR) measurements were employed on a homemade fixed-bed device. The high-purity gas flow of 5 % H_2 balanced by N_2 (30 ml min^{-1}) was added into the reaction bed in the temperature range of 50–650 °C at a heating rate of 5 °C min^{-1} . The consumption signal of H_2 was recorded by a thermal conductivity detector (TCD). X-ray photoelectron spectra (XPS) and valence band spectroscopy (VBS) were obtained on a Thermo Scientific K-Alpha spectrometer using the X-ray source of an Al $\text{K}\alpha$ anode ($h\nu = 1486.6$ eV). The binding energy scale was referenced by the carbon at 284.8 eV. The deconvolutions area of the V $2p_{3/2}$ and O $1s$ spectrum was calculated by Gaussian–Lorentzian curve-fitting method. In-situ XRD was performed in the range of 25–40°, and patterns were obtained by a powder X-ray diffractometer (Rigaku U IV). The temperature of catalysts is controlled by an IR radiant heater. To observe the transient change of VO_x during reduction, the XRD patterns were obtained after 5 min the temperature reached the desired value. In-situ Raman was performed on a Horiba HR Evolution spectrometer with excitation wavelengths of 325 nm and 532 nm. The samples were previously pretreated by air at 480 °C for 1 h and purged with N_2 for 1 h. Then, the gas was changed to 5 % propane balanced by N_2 , and Raman spectra were recorded. The in-situ infrared (IR) camera was employed with homemade equipment. The sample was shaped with a circular mold with a thermocouple inside the catalyst, which could ensure that the catalyst powder distributes evenly. Meanwhile, a xenon lamp was fixed directly above the catalysts. An IR camera tested the surface temperatures of catalysts under light irradiation (wavelength: 320–780 nm, light intensity of 350 mW cm^{-2}). The schematic diagram of the device is listed in Fig. S1. The profiles of XPS, VBS, and in-situ IR cameras were obtained through the characterization of reduced catalysts. To simulate the reduced condition, all $\text{VO}_x/\text{Al}_2\text{O}_3$ catalysts were pretreated by C_3H_8 ($\text{C}_3\text{H}_8/\text{N}_2$ is 1/19) at 480 °C for 30 min.

2.3. Catalytic tests for photothermal PDH

The catalytic performances of the catalysts for photothermal PDH were evaluated in a quartz fixed-bed reactor under atmospheric pressure. The catalyst (particle size of 60–80 meshes) was packed inside the flat quartz window and fixed by quartz wool at both ends. The reactor was heated to 480 °C under N_2 , and then the reaction gas was fed with a

weight hourly space velocity (WHSV) of 0.86 h^{-1} (the ratio of $\text{C}_3\text{H}_8/\text{N}_2$ is 1/19). A Xenon lamp (Micro solar 300 from Perfect Light Inc.) provided light radiation (wavelength: 320–780 nm, light intensity: 300 mW cm^{-2}). The installation diagram of the reactor is displayed in Fig. S2. Exhaust gases were analyzed using an online GC (SP-3420) equipped with a flame ionization detector (HP-PLOT/Q) and a thermal conductivity detector (TDX-01). Noteworthy, the $\text{VO}_x/\text{Al}_2\text{O}_3$ catalysts show an induction period at the beginning of the reaction. $\text{VO}_x/\text{Al}_2\text{O}_3$ catalysts exhibit a high activity but soon decreases during 30 min, which is due to the residual surface oxygen. After the induction process, the carbon atom balance was higher than 90 % during the whole reaction process. The propane conversion is controlled in the reaction kinetics-limited regime to eliminate the mass-transfer effect. The diffusion analyses were carried out, and the results are shown in the Supplement Information. The propane conversion and selectivity were calculated through Eq. (2) and Eq. (3). The catalytic stability tests were carried out under a similar reaction method, except that the WHSV is 0.4 h^{-1} (the ratio of $\text{C}_3\text{H}_8/\text{N}_2$ is 1/14).

$$\text{Conv} (\%) = 100 * ([\text{FC}_3\text{H}_8]_{\text{inlet}} - [\text{FC}_3\text{H}_8]_{\text{outlet}}) / [\text{FC}_3\text{H}_8]_{\text{inlet}} \quad (2)$$

$$\text{Selec} (\%) = 100 * [\text{FC}_3\text{H}_6]_{\text{inlet}} / ([\text{FC}_3\text{H}_8]_{\text{inlet}} - [\text{FC}_3\text{H}_8]_{\text{outlet}}) \quad (3)$$

The first-order deactivation constant (K_d) was calculated by Eq. (4), which are generally used in recent studies [25].

$$K_d = (\ln[(1 - \text{Conv}_{\text{initial}}) / \text{Conv}_{\text{initial}}] - \ln[(1 - \text{Conv}_{\text{final}}) / \text{Conv}_{\text{final}}]) / t \quad (4)$$

The apparent activation energy (E_a) was calculated by Arrhenius plots at 440, 480, 520, and 560°C with a WHSV of $2.4\text{--}0.6 \text{ h}^{-1}$, while the propane conversion is below 10 %.

2.4. DFT Calculation

The electronic distribution over $\text{VO}_x/\text{Al}_2\text{O}_3$ and V_2O_5 catalysts was calculated by density functional theory (DFT). The bare Al_2O_3 model was built by the cut along (110) plane of $\gamma\text{-Al}_2\text{O}_3$. Monomeric VO_4 and dimeric V_2O_5 were loaded on the surface of the Al_2O_3 model to construct a model of $\text{VO}_x/\text{Al}_2\text{O}_3$ catalyst with isolated and polymeric VO_x . According to the result of in-situ UV-Raman, the V=O bonds are broken to simulate the PDH condition. The bulk V_2O_5 model was built by the cut along (0001) plane of $\alpha\text{-V}_2\text{O}_5$. The calculations were operated by the Vienna ab initio simulation package (VASP) software. The generalized gradient optimization (GGA)-Perdew Burke Ernzerhof (PBE) function with the Ueff parameter of 3.2 eV was used in the calculation process.

3. Results and discussions

3.1. Structural properties of as-prepared $\text{VO}_x/\text{Al}_2\text{O}_3$

According to the principle of spontaneous mono-layer distribution, VO_x species mainly exist as the mono-layer isolated and polymeric structure at low vanadium concentration, while it aggregates to V_2O_5 spontaneously to reduce its surface energy at high vanadium concentration [26]. To detect the crystal phase structure, XRD patterns of $\text{VO}_x/\text{Al}_2\text{O}_3$ catalysts were employed. As shown in Fig. 1A, the diffraction peak located at 45.8 and 66.8° can be indexed to (400) and (440) crystal facets of $\gamma\text{-Al}_2\text{O}_3$ (PDF#79-1558), respectively. For the low loading amounts (1–10 wt%) of VO_x species, only characteristic peaks of $\gamma\text{-Al}_2\text{O}_3$ were detected, indicating that mono-layer VO_x is well dispersed on the surface of $\gamma\text{-Al}_2\text{O}_3$ support. For $\text{VO}_x/\text{Al}_2\text{O}_3\text{-15}$ catalyst, the characteristic peaks of V_2O_5 at 15.4 , 20.3 , and 26.2° appear, which is matched to (200), (001), and (110) facet of orthorhombic crystal phase with a Pmmn59 symmetry (PDF#77-2418), respectively [27]. With increasing

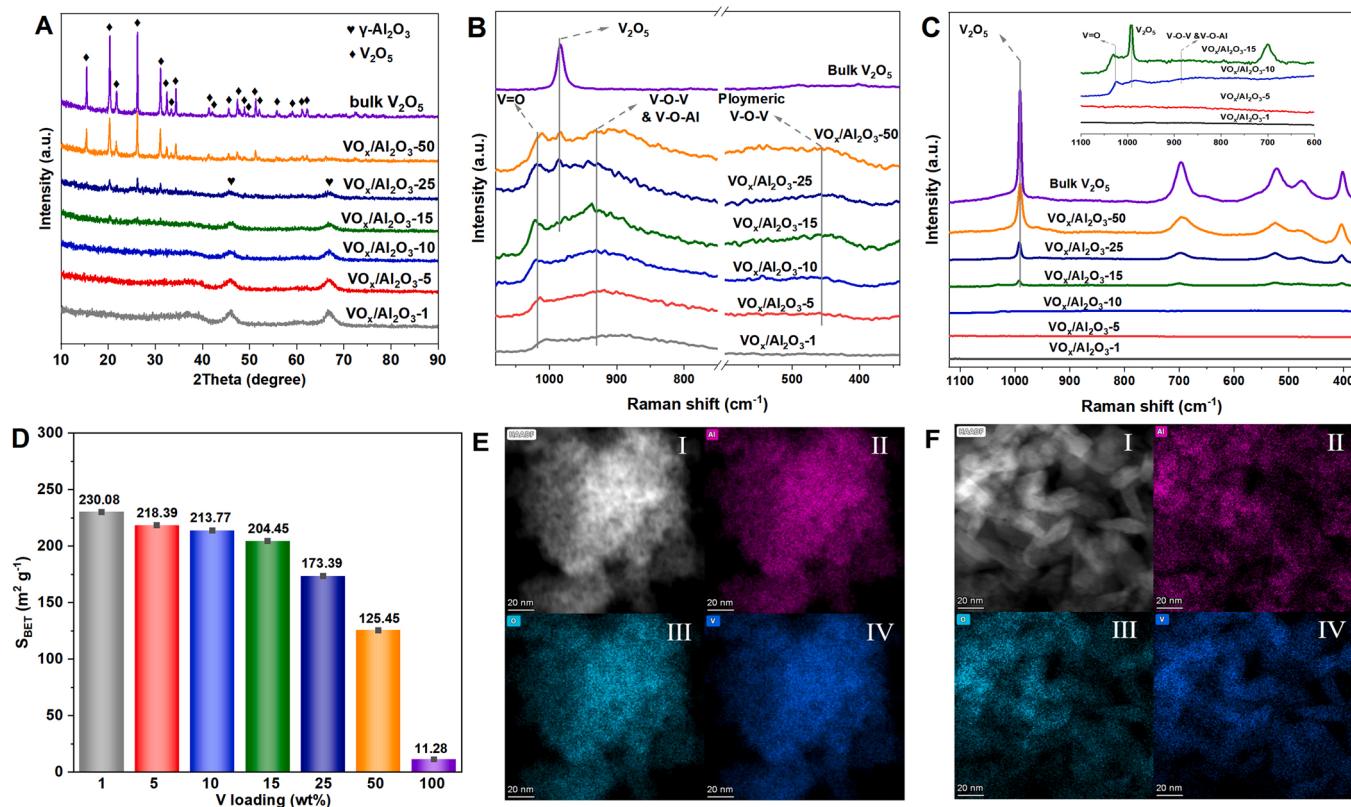


Fig. 1. XRD patterns (A), Raman spectra (B-C), and specific surface areas (D) of fresh $\text{VO}_x/\text{Al}_2\text{O}_3$ catalysts. The exciting wavelength in (B) and (C) Raman spectra is 325 and 532 nm, respectively. HR-STEM and corresponding element mapping of $\text{VO}_x/\text{Al}_2\text{O}_3\text{-15}$ catalyst (E) and $\text{VO}_x/\text{Al}_2\text{O}_3\text{-50}$ catalyst (F). STEM image (I), element mapping of Al atoms (II), O atoms (III), and V atoms (IV).

VO_x loading amounts, the intensity ratio of the XRD peak of (001) facet to other facets gradually enhances, indicating that 2D mono-layer VO_x grows along the c-axis into the 3D V_2O_5 component.

UV-Raman spectra excited by a 325 nm laser were applied to determine the surface state of the supported VO_x component. As shown in Fig. 1B, Raman peaks at 930 and 1018 cm^{-1} are assigned to the stretching vibration of V-O-M bonds (V-O-V or V-O-Al bonds) and V=O bonds, respectively [28]. $\text{VO}_x/\text{Al}_2\text{O}_3$ -n catalysts ($n > 1$) show one weak characterized Raman peak at 456 cm^{-1} , which is attributed to the stretching vibration of polymeric V-O-V bonds. However, the peak of the $\text{VO}_x/\text{Al}_2\text{O}_3$ -1 catalyst is not observed, indicating that isolated VO_x is dominantly present on the surface of $\gamma\text{-Al}_2\text{O}_3$ support. The characterized peak of $\text{VO}_x/\text{Al}_2\text{O}_3$ -n catalysts ($n > 5$) at 456 cm^{-1} gradually strengthens, indicating that a polymeric VO_x mono-layer is increasingly formed. For $\text{VO}_x/\text{Al}_2\text{O}_3$ -n catalysts ($n > 25$), one new Raman peak at 985 cm^{-1} is observed, which is assigned to the stretching vibration of V=O bonds of bulk V_2O_5 nanocrystal [29]. To detect detailed structure information of the V_2O_5 component, Raman spectra with an exciting wavelength of 532 nm are employed. As shown in Fig. 1C, $\text{VO}_x/\text{Al}_2\text{O}_3$ -10 catalyst exhibits one strong characterized peak of polymeric VO_x at 1024 cm^{-1} and one weak shoulder of V_2O_5 at 990 cm^{-1} , indicating that the mono-layer VO_x and V_2O_5 species co-exist on the surface of Al_2O_3 support. Compared to the $\text{VO}_x/\text{Al}_2\text{O}_3$ -10 catalyst, the Raman characterized peak of $\text{VO}_x/\text{Al}_2\text{O}_3$ -15 catalyst at 990 cm^{-1} is stronger obviously than that of polymeric VO_x , indicating that the V_2O_5 nanocrystal is the dominant surface species of VO_x component. As shown in Fig. S3, with increasing VO_x loading amounts, the Raman characteristic peak at 990 cm^{-1} shifts gradually to the low wavenumber region, which can be attributed to a decrease in the oxygen defects induced by the formation of V_2O_5 nanocrystal. Combining the results of XRD and Raman, the mono-layer isolated and polymeric VO_x species in the $\text{VO}_x/\text{Al}_2\text{O}_3$ -n catalyst ($n < 10$) is the dominant surface state, while the V_2O_5 nanocrystal in the $\text{VO}_x/\text{Al}_2\text{O}_3$ -n catalyst ($n > 10$) is dominant.

The surface property and pore structure of $\text{VO}_x/\text{Al}_2\text{O}_3$ catalysts are investigated by the N_2 adsorption-desorption test. As shown in Fig. S4, all $\text{VO}_x/\text{Al}_2\text{O}_3$ catalysts exhibit the IV-type isotherm with an H1 hysteresis loop, which is attributed to the capillary condensation in mesopores. Furthermore, the specific surface area (S_{BET}) values of $\text{VO}_x/\text{Al}_2\text{O}_3$ catalysts were obtained by the Brunauer–Emmett–Teller method. As shown in Table S1 and Fig. 1D, the $\text{VO}_x/\text{Al}_2\text{O}_3$ -1 catalyst with isolated VO_x species exhibits the highest S_{BET} value, which is 230.08 $\text{m}^2 \text{g}^{-1}$. After the formation of the polymeric VO_x , their S_{BET} values have not obvious change. The S_{BET} value of the $\text{VO}_x/\text{Al}_2\text{O}_3$ -5 catalyst is 218.39 $\text{m}^2 \text{g}^{-1}$, while that of the $\text{VO}_x/\text{Al}_2\text{O}_3$ -10 catalyst is 213.77 $\text{m}^2 \text{g}^{-1}$. However, the formation of V_2O_5 nanocrystals in $\text{VO}_x/\text{Al}_2\text{O}_3$ -n catalysts ($n > 10$) obviously decrease the S_{BET} value, and the values of $\text{VO}_x/\text{Al}_2\text{O}_3$ -25 and $\text{VO}_x/\text{Al}_2\text{O}_3$ -50 catalysts are 173.39 and 125.45 $\text{m}^2 \text{g}^{-1}$, respectively. The catalysts with mono-layer VO_x show higher S_{BET} than V_2O_5 -abundant catalysts, which is attributed to the 3D V_2O_5 nanocrystals blocking the mesoporous of Al_2O_3 support. The morphologies of $\text{VO}_x/\text{Al}_2\text{O}_3$ catalyst were also characterized by HAADF-STEM and corresponding element mapping. As shown in Fig. 1E, V, Al, and O elements are dispersed in a similar region of $\text{VO}_x/\text{Al}_2\text{O}_3$ -15 catalyst, indicating that VO_x evenly covers the whole support. There is no V_2O_5 nanocrystals being observed, which can be attributed to the low contrast between V and Al elements and the small size of V_2O_5 nanoparticles. As shown in Fig. 1F, rhombic-shaped crystals with uniform distribution can be observed on the $\text{VO}_x/\text{Al}_2\text{O}_3$ -50 catalyst, which can be assigned to orthorhombic V_2O_5 nanocrystals with good crystallinity.

The light absorption efficiency of $\text{VO}_x/\text{Al}_2\text{O}_3$ catalysts was measured by the UV–VIS–NIR spectra. As shown in Fig. S5, $\text{VO}_x/\text{Al}_2\text{O}_3$ catalysts exhibit multiple overlapping absorption bands ranging from 200 to 500 nm, which originates from the ligand-to-metal charge transfer (LMCT) of O^{2-} to V^{5+} . The absorption bands at 228, 270 nm, and 379 nm are assigned to isolated VO_4 , low polymeric VO_4 , and highly polymeric VO_4 or VO_5 , respectively. And the absorption band at 455 nm belongs to

octahedrally VO_6 in bulk V_2O_5 nanocrystal [30]. For $\text{VO}_x/\text{Al}_2\text{O}_3$ -n catalysts ($n > 15$), the formation of V_2O_5 weakens UV light adsorption but improve adsorption for visible light, which is attributed to the aggregation of polymeric VO_x into V_2O_5 nanocrystals. In addition, the adsorption band at 500–1200 nm is assigned to the d-d transition. Compared to LMCT bands, the mono-layer $\text{VO}_x/\text{Al}_2\text{O}_3$ catalysts exhibit weak adsorption bands of d-d transition, which is attributed to the empty 3d orbital of V^{5+} ions. However, V_2O_5 -abundant catalysts have the extended adsorption band of d-d transition, which are assigned to oxygen defects in nano-scale V_2O_5 crystals charging electrons in the 3d orbit of V^{5+} ions [31]. The mono-layer VO_x species exhibits stronger light adsorption in UV light than V_2O_5 , while V_2O_5 shows an advantage in the absorption of VIS light compared with mono-layer VO_x .

The dispersion of VO_x can be described quantitatively by its band gap energy (E_g) value [32]. As shown in Figs. S6 (A–G), the E_g value of $\text{VO}_x/\text{Al}_2\text{O}_3$ catalysts was calculated by the Kubelka–Munk function. For polymerized VO_x , V-O-V bonds can overlap their electron orbitals and thus reduce binding energy, while isolated VO_x without any V-O-V bonds shows the highest binding energy. Therefore, the number of V-O-V bonds for a supported VO_x catalyst can be determined by internal standards using vanadium compounds with known number of V-O-V bonds [33]. The correlation line between E_g values and the number of V-O-V bonds is shown in Fig. S7. The $\text{VO}_x/\text{Al}_2\text{O}_3$ -1 catalyst shows the highest E_g value (3.97 eV), indicating the atomically dispersed VO_x without any V-O-V bonds. The E_g value of the $\text{VO}_x/\text{Al}_2\text{O}_3$ -10 catalyst is 3.48 eV, indicating that VO_x has one or two adjoining VO_x sites. The E_g values of V_2O_5 -abundant catalysts are lower than that of mono-layer catalysts. The lowest E_g value (2.76 eV) is for the $\text{VO}_x/\text{Al}_2\text{O}_3$ -50 catalyst, which is characteristic of highly polymerized VO_5 or VO_6 with more than three V-O-V bonds. In sum, the mono-layer VO_x components have obvious advantages in S_{BET} value and VO_x dispersion compared to V_2O_5 nanocrystals.

3.2. Light-driven photothermal catalytic performance for PDH

A fixed-bed reactor with a xenon lamp was used to carry out the photothermal PDH reaction of catalysts, which allowed for stable photon flux and temperature control. As shown in Fig. 2(A and B), the tests were alternately employed under dark and irradiation to identify the role of light. In the absence of light irradiation, the $\text{VO}_x/\text{Al}_2\text{O}_3$ catalysts show poor propane conversion ($< 4.2\%$). A remark enhancement in propane conversion is obtained once the catalyst is under light irradiation. Under irradiation with an intensity of 300 mW cm^{-2} , the propane conversion of the $\text{VO}_x/\text{Al}_2\text{O}_3$ -25 catalyst is 1.77-fold that of the absence of light irradiation, while its selectivity slightly decreases due to the increasing concentration of propylene [34]. The same propane conversion level in the thermal process would require about 40 °C higher temperature than in the photothermal process. The propane conversion returns to its original value once the irradiation was turned off, indicating that the promoting effect of light is reversible. Fig. 2C shows the propane conversion rate of the $\text{VO}_x/\text{Al}_2\text{O}_3$ -25 catalyst as a function of light intensity. The propane conversion rate increases gradually with the strengthening of light intensity from 180 to 300 mW cm^{-2} . The light intensity well correlates with the propane conversion rate, indicating that the PDH reaction can be promoted by both photo and thermal.

It should be noted that VO_x is supported by chemically and optically inert $\gamma\text{-Al}_2\text{O}_3$ [35]. For this reason, the photocatalytic activity can be ascribed to the VO_x component. Fig. 2D shows the propane conversion rate under dark and irradiation as a function of VO_x loading amounts. For the thermal process, the increasing of VO_x loading in mono-layer $\text{VO}_x/\text{Al}_2\text{O}_3$ -n catalysts ($n < 10$) favors the enhancing propane conversion rate, but that of V_2O_5 -abundant $\text{VO}_x/\text{Al}_2\text{O}_3$ -n catalysts ($n > 15$) still unchanged. The higher propane conversion rate is mainly attributed to abundant VO_x exposed on the catalyst surface with increasing VO_x loading amounts. By extrapolating the propane conversion rate, the

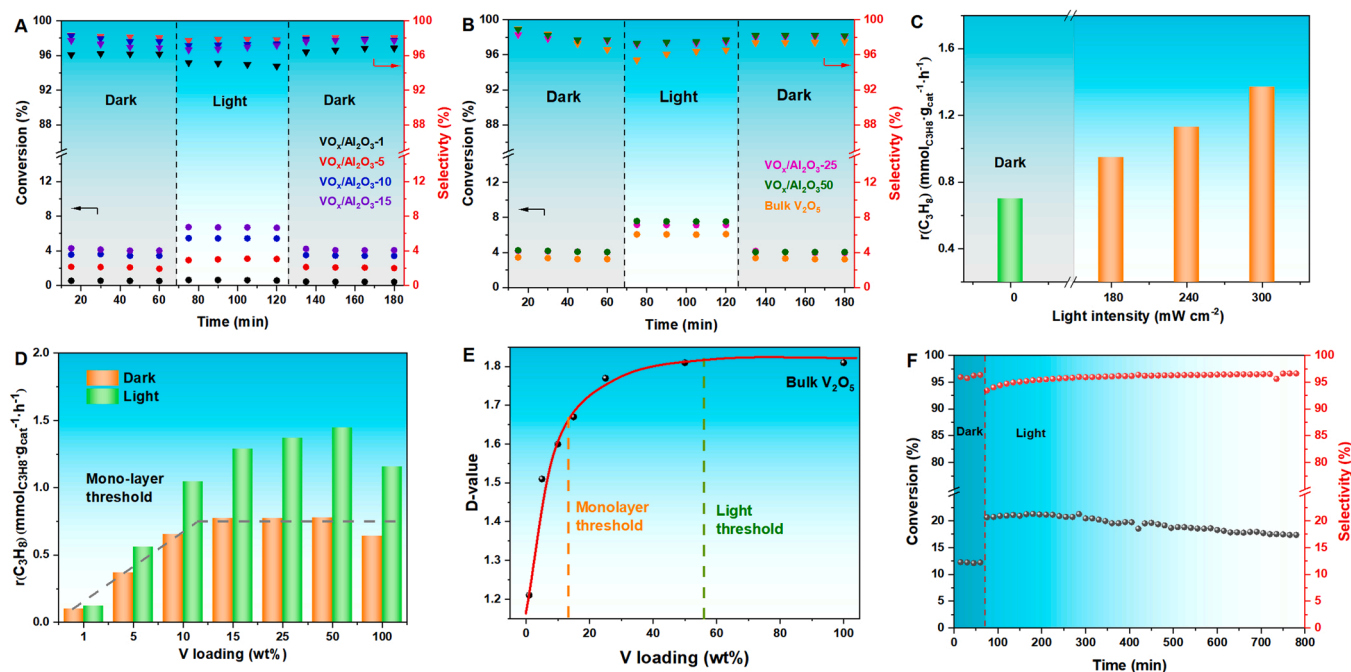


Fig. 2. Photothermal PDH catalytic performance over $\text{VO}_x/\text{Al}_2\text{O}_3$ catalysts: propane conversion and stability at 480°C (A, B), the propane conversion rate of $\text{VO}_x/\text{Al}_2\text{O}_3$ -25 catalyst as a function of light intensity (C), the propane conversion rate as a function of VO_x loading amounts (D), the corresponding photothermal efficiency (D-value) (E), and long-term stability test of $\text{VO}_x/\text{Al}_2\text{O}_3$ -25 catalyst for PDH (F).

intersection at ~ 12 wt % is identified as the mono-layer dispersion threshold, in which the VO_x mono-layer completely covers the whole support. Over this threshold, the superfluous VO_x component aggregate into 3D V_2O_5 nanocrystal, which decreases exposed active sites and propane conversion of catalysts. However, under irradiation, a high VO_x loading not only favor conversion rate of mono-layer catalysts but also notably promote that of V_2O_5 -abundant catalysts. The propane conversion rate increases gradually with increasing of VO_x loading amount until 50 wt%. The V_2O_5 -abundant $\text{VO}_x/\text{Al}_2\text{O}_3$ -50 catalyst shows a 1.4-fold conversion rate than $\text{VO}_x/\text{Al}_2\text{O}_3$ -10 catalyst dominated by polymeric VO_x . The present result infers a totally different effect of the V_2O_5 component between irradiation and dark. Although the V_2O_5 nanocrystal plays a negative role in the thermal process, it unexpectedly promotes the photothermal process.

During the photothermal catalytic process, the catalyst can adsorb incident photons to activate the reactant molecule, and the strength is defined as photothermal efficiency per active site [36]. As V_2O_5 -abundant catalysts have no advantage in exposed active sites, the photothermal efficiency possibly accounts for improved photothermal PDH activity. Therefore, the D-value (a ratio of TOF under irradiation to dark) of the $\text{VO}_x/\text{Al}_2\text{O}_3$ catalyst was calculated, which is the widely used index of photothermal efficiency [14,37]. As shown in Fig. 2E, the D-value increases gradually with increasing VO_x loading amounts. The D-value of the $\text{VO}_x/\text{Al}_2\text{O}_3$ -1 catalyst is only 1.21, while that of the $\text{VO}_x/\text{Al}_2\text{O}_3$ -15 catalyst is 1.67. The D-value of the $\text{VO}_x/\text{Al}_2\text{O}_3$ -50 catalyst is the highest at 1.81, which is similar to the bulk V_2O_5 catalyst. The increased D-value correlates well with the photothermal PDH conversion. Thus, the high catalytic activity of V_2O_5 -abundant catalysts for PDH can be attributed to the improved photothermal synergy effect. In addition, the D-value rises in order of isolated VO_x , polymeric VO_x , and V_2O_5 , which exhibits an obvious structure-depending photothermal efficiency.

To investigate the functional performance of the photothermal catalyst, the long-term stability test of the $\text{VO}_x/\text{Al}_2\text{O}_3$ -25 catalyst was carried out. As shown in Fig. 2F, under irradiation, the initial propane conversion of the $\text{VO}_x/\text{Al}_2\text{O}_3$ -25 catalyst is 20.7 %. In addition, $\text{VO}_x/\text{Al}_2\text{O}_3$ -25 catalyst also shows robust stability during the 12 h reaction, and its deactivation constant (K_d) value is only 0.018 h^{-1} . Therefore,

$\text{VO}_x/\text{Al}_2\text{O}_3$ -25 catalyst has good catalytic performance in terms of activity and stability for PDH reaction. The catalytic stability is a critical factor in industrial applications, while coke presents as the crucial reason for deactivation in PDH. Coke deposition is a typical structure-sensitive reaction. A stable vanadium-based catalyst for PDH should consist of spatially isolated VO_x sites to avoid C-C bond coupling or deep dehydrogenation in the formation of coke [38]. The catalyst with ultra-low VO_x loading amounts can obtain atomically dispersed active sites but limits its activity. For photothermal PDH, the $\text{VO}_x/\text{Al}_2\text{O}_3$ -25 catalyst with abundant highly polymeric V_2O_5 exhibits high activity and robust stability, which can be attributed to the heat-induced coke deposition reaction avoided by the low-temperature reaction. In addition, the catalytic performance between $\text{VO}_x/\text{Al}_2\text{O}_3$ -25 catalyst under irradiation and industrial $\text{PtSn}/\text{Al}_2\text{O}_3$ catalyst were further compared at 480°C . As shown in Fig. S8, the $\text{VO}_x/\text{Al}_2\text{O}_3$ -25 catalyst show a higher conversion and selectivity than industrial $\text{PtSn}/\text{Al}_2\text{O}_3$ catalyst, which indicate $\text{VO}_x/\text{Al}_2\text{O}_3$ catalytic system has a good prospect of industrial application under photothermal conditions. In sum, light irradiation can improve the activity of the $\text{VO}_x/\text{Al}_2\text{O}_3$ catalysts for PDH, in which VO_x works as a photothermal active component. The photothermal catalytic performance is highly dependent on the surface state of VO_x , and the V_2O_5 nanocrystal shows higher photothermal efficiency than polymeric and isolated VO_x .

3.3. In-situ structure transformation of $\text{VO}_x/\text{Al}_2\text{O}_3$ catalysts

Molecule adsorption or chemical reaction can reconstruct oxide into a particular structure. Under the oxidizing environment, 2D polymeric VO_x would aggregate into low-energy 3D V_2O_5 with increasing VO_x loading amounts. The 3D V_2O_5 crystal is formed by 2D VO_x layers stacking along the c-axis, which are only connected by weak van der Waals forces [26]. Thus, the 3D structure of V_2O_5 can be distorted even under a mild reduction environment [39]. To investigate the phase structure stability of the catalysts in the PDH reaction, XRD was conducted to analyze the crystal structure of the reduced $\text{VO}_x/\text{Al}_2\text{O}_3$ catalyst. As shown in Fig. 3(A and B), there is no change in characterized peaks of $\gamma\text{-Al}_2\text{O}_3$ after the PDH reaction, but the peak assigned to the

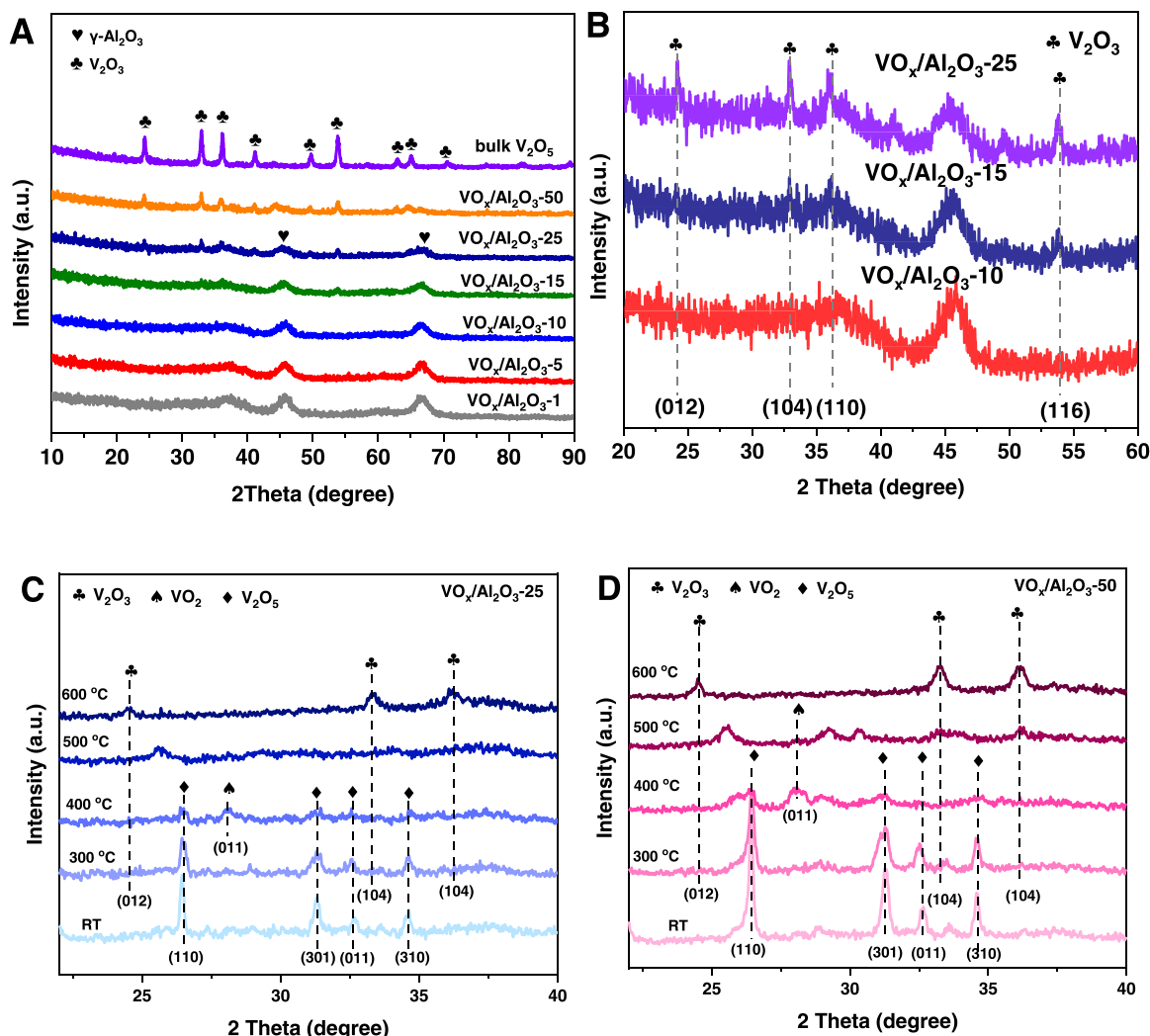


Fig. 3. XRD patterns (A) and its enlarged pattern (B) of used $\text{VO}_x/\text{Al}_2\text{O}_3$ catalysts; In-situ XRD of $\text{VO}_x/\text{Al}_2\text{O}_3$ -25 (C) and $\text{VO}_x/\text{Al}_2\text{O}_3$ -50 (D) catalysts.

V_2O_5 completely disappears. As a substitute, the new characteristic peaks appear at 24.3° , 33.0° , 36.3° , and 53.9° , which are assigned to the (012), (104), (110), and (116) crystal facets of rhombohedral V_2O_3 crystals (PDH#74–0325), respectively [40]. As shown in Table S2, the in-situ formed V_2O_3 nanocrystal has smaller particle sizes than the fresh V_2O_5 nanocrystal, indicating that the V_2O_5 nanocrystal is dispersed in the atmosphere condition of propane. To monitor the transformation process of V_2O_5 nanocrystals, the in-situ temperature-resolved (TR) XRD was measured during the propane condition. As shown in Fig. 3(C and D), the V_2O_5 nanocrystals in the $\text{VO}_x/\text{Al}_2\text{O}_3$ -25 and $\text{VO}_x/\text{Al}_2\text{O}_3$ -50 catalysts are the dominant component under room temperature. The characteristic peaks of V_2O_5 nanocrystals decrease and widen onward 300°C under a propane atmosphere, indicating that V_2O_5 crystals are dispersed and transformed to the XRD-insensitive phase, which may be amorphous polymeric VO_x . At 400°C , there are only very weak diffraction peaks, which are assigned to surface V_2O_5 and V_2O_4 nanocrystals. At 500°C , the peaks of the XRD pattern corresponding to V_2O_3 appear in $\text{VO}_x/\text{Al}_2\text{O}_3$ -50 catalyst, and even the peaks of V_2O_5 completely disappear. The peak intensity of V_2O_3 further increases at 600°C , indicating that V_2O_3 nanocrystals precipitated gradually from amorphous VO_x . In-situ XRD confirms the dispersion-recrystallization process that happened in the V_2O_5 nanocrystal during the PDH reaction. The in-situ transformation of V_2O_5 is seemingly the essential reason for the high photothermal activity of V_2O_5 -abundant catalysts.

To reveal the actual active site during the PDH reaction, the in-situ

UV-Raman spectra were carried out, and the results are shown in Fig. 4. Fig. 4A shows Raman spectra of mono-layer $\text{VO}_x/\text{Al}_2\text{O}_3$ -n catalysts ($n \leq 10$). Polymeric VO_x is the main structure in the $\text{VO}_x/\text{Al}_2\text{O}_3$ -10 catalyst under oxidizing conditions. Raman peaks at 924 and 1015 cm^{-1} are observed, which are characteristic peaks of V-O-M (V-O-V&V-O-Al) and V=O bonds, respectively. Under PDH condition, the presence of the propane atmosphere results in a remarkable decrease of peak intensity at 1015 cm^{-1} , which is attributed to V=O bonds reduced by propane. However, there is barely any change in the peak of V-O-M bonds. Thus, the polymeric structure of VO_x species is still stable during the PDH condition. The red shift in the peak of V-O-M bonds can be attributed to the decreased valence of V^{5+} ions, which can weaken the interaction between center V^{5+} ions and coordinated O^{2-} ions [41]. The reduced $\text{VO}_x/\text{Al}_2\text{O}_3$ -5 catalyst shows a similar Raman pattern with the reduced $\text{VO}_x/\text{Al}_2\text{O}_3$ -10 catalyst, indicating that polymeric VO_x is the dominant component. For reduced $\text{VO}_x/\text{Al}_2\text{O}_3$ -1 catalyst, the characteristic peaks disappear completely. At extremely low VO_x concentrations, the isolated V^{5+} ions would be anchored by the lattice defects of $\gamma\text{-Al}_2\text{O}_3$ support, and the strong interaction of V-O-Al bonds leads to the low Raman activity of V^{5+} ions [42]. Thus, the isolated VO_x species hardly displays the Raman peaks.

The in-situ UV-Raman spectra of $\text{VO}_x/\text{Al}_2\text{O}_3$ -n catalysts ($n \geq 15$) are shown in Fig. 4B. Under the oxidized conditions, except for characteristic peaks assigned to V=O and V-O-M bonds, the Raman pattern of $\text{VO}_x/\text{Al}_2\text{O}_3$ -15 catalyst shows an additional shoulder at 971 cm^{-1} , which

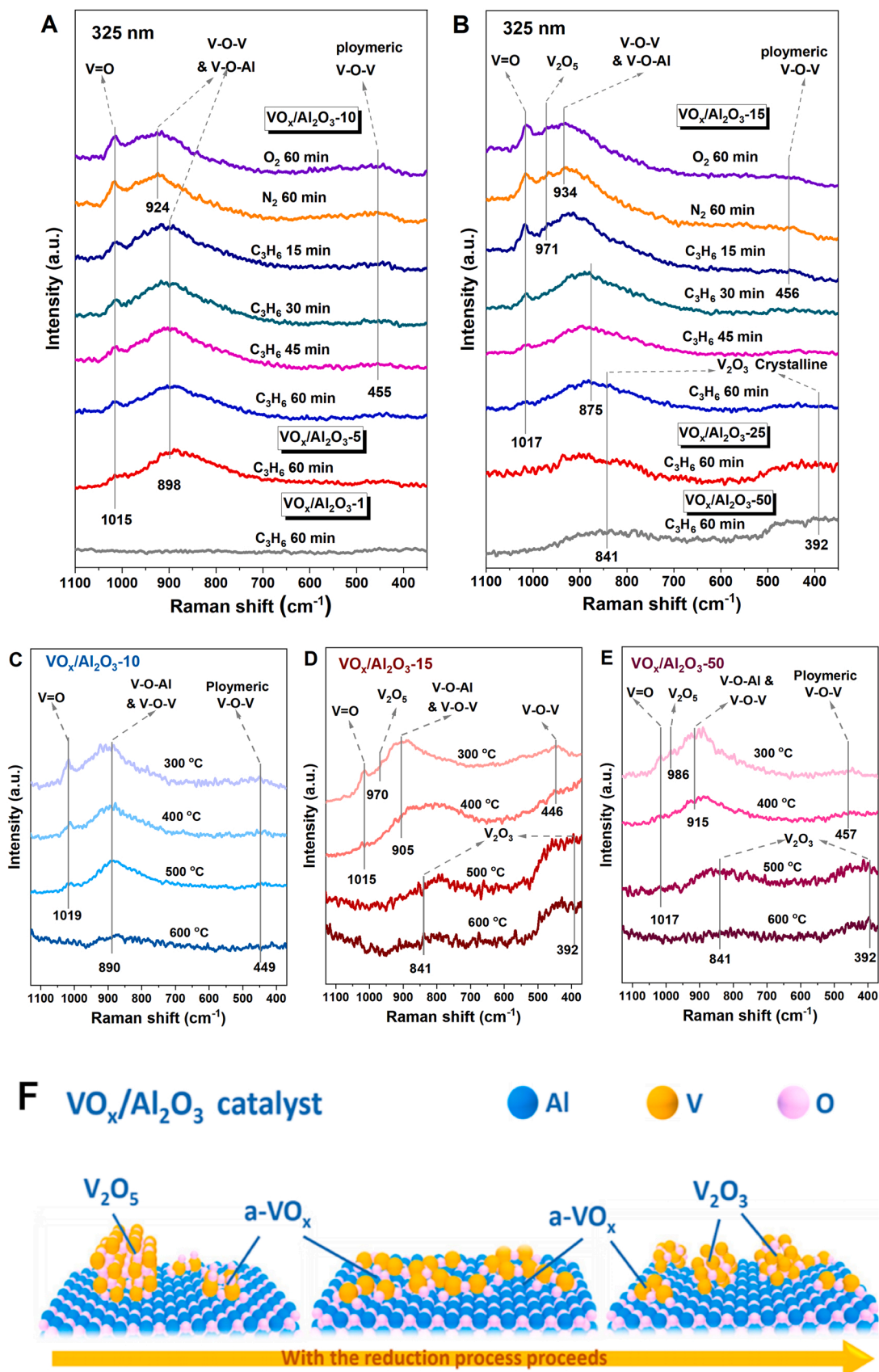


Fig. 4. In situ UV-Raman (325 nm excitation) spectra of $\text{VO}_x/\text{Al}_2\text{O}_3$ catalysts with the evolution of reaction time (A, B) and temperature (C, D, E). The structural transformation mechanism diagram of surface VO_x species (F). The a- VO_x is the short name for amorphous VO_x . (Orange, V atoms; Pink, O atoms; Blue, Al atoms).

is attributed to the bulk V_2O_5 crystal. Upon exposure to propane, the peak intensity of V_2O_5 decreases with a concomitant increase in the intensity of V-O-M bonds, indicating that V_2O_5 crystals transform into polymeric VO_x . The peak intensity of $V=O$ bonds at 1017 cm^{-1} declines and completely disappears after 60 min propane treatment. Meanwhile, the Raman peaks of the V-O-V bond at 934 and 456 cm^{-1} shift to the low wavenumber range, indicating that the reconstruction happened in V-O-Al and V-O-V bonds of polymeric VO_x . As shown in Fig. S9, the UV-Raman spectra of the bulk V_2O_5 show two peaks at 392 and 841 cm^{-1} . Thus, the change of Raman peak can be assigned to polymeric VO_x reconstructed into V_2O_3 nanocrystals [43]. Noteworthy, Raman peaks of the reduced VO_x/Al_2O_3 -25 and VO_x/Al_2O_3 -50 catalysts are located at lower wavenumber range than VO_x/Al_2O_3 -15 catalyst, which indicate more V_2O_3 nanocrystals are formed. The photothermal efficiency (D-value) increases gradually with increasing VO_x loading amounts until 50 wt%. Combined with the result of in-situ XRD and Raman, the V_2O_3 component seems to play an essential role in increasing photothermal efficiency for PDH reaction.

To further investigate the transformation process of V_2O_5 , Fig. 4(C, D, and E) show in-situ Raman spectra of VO_x/Al_2O_3 -10, VO_x/Al_2O_3 -15, and VO_x/Al_2O_3 -50 catalysts with rising temperature, respectively. With increasing reaction temperature, the characterized peaks at 1018 , 890 , and 449 cm^{-1} over VO_x/Al_2O_3 -10 catalyst gradually decrease but do not shift significantly, indicating that polymeric VO_x is still the dominant component. For V_2O_5 -abundant VO_x/Al_2O_3 -15 and VO_x/Al_2O_3 -50 catalysts, the characteristic peaks of polymeric VO_x and V_2O_5 at ~ 910 and $\sim 980\text{ cm}^{-1}$ co-exist at 300°C . At 400°C , the Raman peak of VO_x/Al_2O_3 -15 and VO_x/Al_2O_3 -50 catalysts at $\sim 920\text{ cm}^{-1}$ shift to $\sim 880\text{ cm}^{-1}$, indicating that the polymeric VO_x and V_2O_3 co-exist. Above 500°C , only characteristic peaks of V_2O_3 can be observed in VO_x/Al_2O_3 -50. Thus, the polymeric VO_x is the intermediate component in the transformation of V_2O_5 to V_2O_3 nanocrystals. According to the result of in-situ UV-Raman, a scheme of the in-situ transformation mechanism of V_2O_5 -abundant catalyst during PDH reaction could be displayed in Fig. 4F. For bulk V_2O_5 crystal, 2D V_xO_y layers are connected by $V=O$ bonds in interlayer space into the 3D structure [44]. During the PDH reaction, propane can induce the breaking of the interbedded $V=O$ bonds, and the V_2O_5 crystal gradually loses its 3D structure and disperses into a 2D polymeric VO_x state. These in-situ formed polymeric VO_x components are unstable at high temperatures, which would be further reconstructed into well-organized 3D V_2O_3 nanocrystals for reducing surface entropy.

The in-situ VIS-Raman was also applied to detect the transformation of V_2O_5 . As shown in Fig. S10, the Raman peaks of V_2O_5 -abundant catalysts entirely disappear after exposure to propane. The Raman characteristic peaks of bulk V_2O_3 were not observed, which can be attributed to the VIS-Raman insensitivity of V_2O_3 nanocrystals. To study the reduction process of VO_x , H_2 -TPR was shown in Fig. S11. VO_x/Al_2O_3 -1 catalyst exhibits two separate reduction peaks at 533°C and 598°C , which is attributed to isolated VO_x anchored by the lattice of Al_2O_3 . The reduction peaks over VO_x/Al_2O_3 -5 and VO_x/Al_2O_3 -10 catalysts shift to the lower temperature region at about 470°C , indicating that isolated VO_x is less reducible than polymerized VO_x . A new reduction peak above 500°C over V_2O_5 -abundant catalysts can be attributed to the consumption of $V=O$ bonds between V_xO_y layers in V_2O_5 . The peak intensity and reduced temperature of H_2 consumption gradually increase with increasing VO_x loading amounts, which is correlated with the formation of the V_2O_3 component.

The in-situ transformation from V_2O_5 to V_2O_3 plays a vital role in promoting the activity of V_2O_5 -abundant catalysts for photothermal PDH. During the processes of PDH, V_2O_5 crystals in V_2O_5 -abundant catalysts are dispersed into the polymeric VO_x , and further reconstructed into highly dispersed V_2O_3 nanocrystals, which effectively enhances exposed active sites. Noteworthy, the monolayer dispersion threshold is also closely related to the formation of V_2O_3 nanocrystals. As shown in Fig. S12, the XRD peak of VO_x/Al_2O_3 catalysts with V loading amount lower than 13 wt% show only a peak attributed to

$\gamma\text{-Al}_2\text{O}_3$, while VO_x/Al_2O_3 -14 catalyst shows a weak peak at 53.9° assigned to V_2O_3 . This indicates that V_2O_3 nanocrystals form at the V loading of 13–14 wt%, which well correlate with the monolayer dispersion threshold obtained by the PDH reaction. In addition, the formation of V_2O_3 is well correlated with D-value, which leads to higher photothermal efficiency than mono-layer VO_x . Thus, the in-situ transformation is the main reason for the V_2O_5 -abundant catalyst possessing high activity for photothermal PDH. For mono-layer VO_x/Al_2O_3 catalysts, the surface state of VO_x has no significant transformation. As VO_x/Al_2O_3 -10 catalyst has a higher D-value than VO_x/Al_2O_3 -1 and VO_x/Al_2O_3 -5 catalysts, polymeric VO_x should be more favorable for photothermal PDH than isolated VO_x .

3.4. Structure-dependent optical properties of VO_x/Al_2O_3 catalysts

The morphology can affect the optical property of catalysts, which is ascribed to the quantal structure effect [45]. The photothermal efficiency of the VO_x component is also highly dependent on its morphology, including isolated VO_x , polymeric VO_x , and V_2O_3 . To reveal the structure-dependent activity of the VO_x component, the XPS were conducted to investigate the electronic nature of vanadium ions and the surrounding oxygen ions. During the PDH condition, V^{5+} ions can be reduced to V^{4+} and V^{3+} ions. For acquiring the valence distribution of V^{k+} , the ratio of each valence was calculated by peak deconvolution of $V\ 2p_{3/2}$. The binding energies at 515.8 , 516.9 , and 517.9 eV can be attributed to V^{3+} , V^{4+} , and V^{5+} ions, respectively. The peak distribution result of VO_x/Al_2O_3 catalysts is shown in Fig. 5(A, B, and C) and Fig. S13. The correlation coefficient (R^2) is approached at 1.0 for all results, indicating a high fitting degree. The valance state of V^{k+} ions in the VO_x/Al_2O_3 -5 catalyst is a mixture of $3+$, $4+$, and $5+$ states, while the V^{4+} ions possess the predominant amount. The VO_x/Al_2O_3 -15 and VO_x/Al_2O_3 -50 catalysts show a higher fraction of V^{3+} ions than the VO_x/Al_2O_3 -5 catalyst, indicating that the morphology of VO_x can affect the valance distribution of V^{k+} ions. The valance distribution of V^{k+} ions as a function of VO_x loading amounts is shown in Fig. 5D. VO_x/Al_2O_3 -1 catalyst with isolated VO_x has the lowest fraction (19.4 %) of V^{3+} ions. VO_x/Al_2O_3 -10 catalyst dominated by polymeric VO_x has a 32.1 % fraction of V^{3+} ions, indicating that V-O-V bonds can facilitate the formation of V^{3+} ions. For isolated VO_x , polymeric VO_x , and V_2O_5 nanocrystals, V^{5+} ions form the VO_x ($x = 4, 5$, or 6) coordination field by coordinating the V-O-M bond and $V=O$ bond. During the PDH process, the reduction of VO_x by hydrocarbon would consume $V=O$ and V-O-M bonds, while the formation of V^{3+} ions in the VO_x/Al_2O_3 catalyst is mainly attributed to the breakage of $V=O$ bonds [46]. For V_2O_5 -abundant catalysts, the $V=O$ bonds are largely consumed during the PDH reaction, which leads to a higher fraction of V^{3+} ions than that of mono-layer catalysts. Among all catalysts, VO_x/Al_2O_3 -50 catalyst has the highest fraction (39.1 %) of V^{3+} ions.

The O 1s XPS are shown in Fig. 5E. The binding energy of O 1s in mono-layer catalysts is located at 531.2 eV , which is attributed to O^{2-} ions directly attached to the Al_2O_3 support. For VO_x/Al_2O_3 -n catalysts ($n \geq 10$), the binding energy gradually shifts to the low-energy region, which is assigned to the formation of V_2O_3 nanocrystals. The O 1s binding energy of the VO_x/Al_2O_3 -15 catalyst is located at 531.1 eV , while that of the VO_x/Al_2O_3 -50 catalyst is located at 530.8 eV . It indicates the additional electron transferring into O^{2-} ions in the V_2O_3 nanocrystal, which can be attributed to electron interaction between V^{3+} ions and O^{2-} ions. The electron-rich V^{3+} ions would play as donors and charge to adjacent O^{2-} ions. In addition, O 1s spectra in VO_x/Al_2O_3 catalysts can be deconvoluted into two peaks: one with binding energy at 531.2 eV is assigned to oxygen atoms in mono-layer VO_x (O_a), and the other with binding energy at 530.6 eV (O_b) to lattice oxygen in V_2O_3 . As shown in Fig. 5E, the O 1s peak of VO_x/Al_2O_3 -n catalysts ($n < 15$) show a good symmetry at 531.2 eV , indicating that VO_x species mainly exist in the form of VO_x monolayer. For VO_x/Al_2O_3 -15, VO_x/Al_2O_3 -25, and VO_x/Al_2O_3 -50 catalysts, the O 1s peak has a poor symmetry, which can be

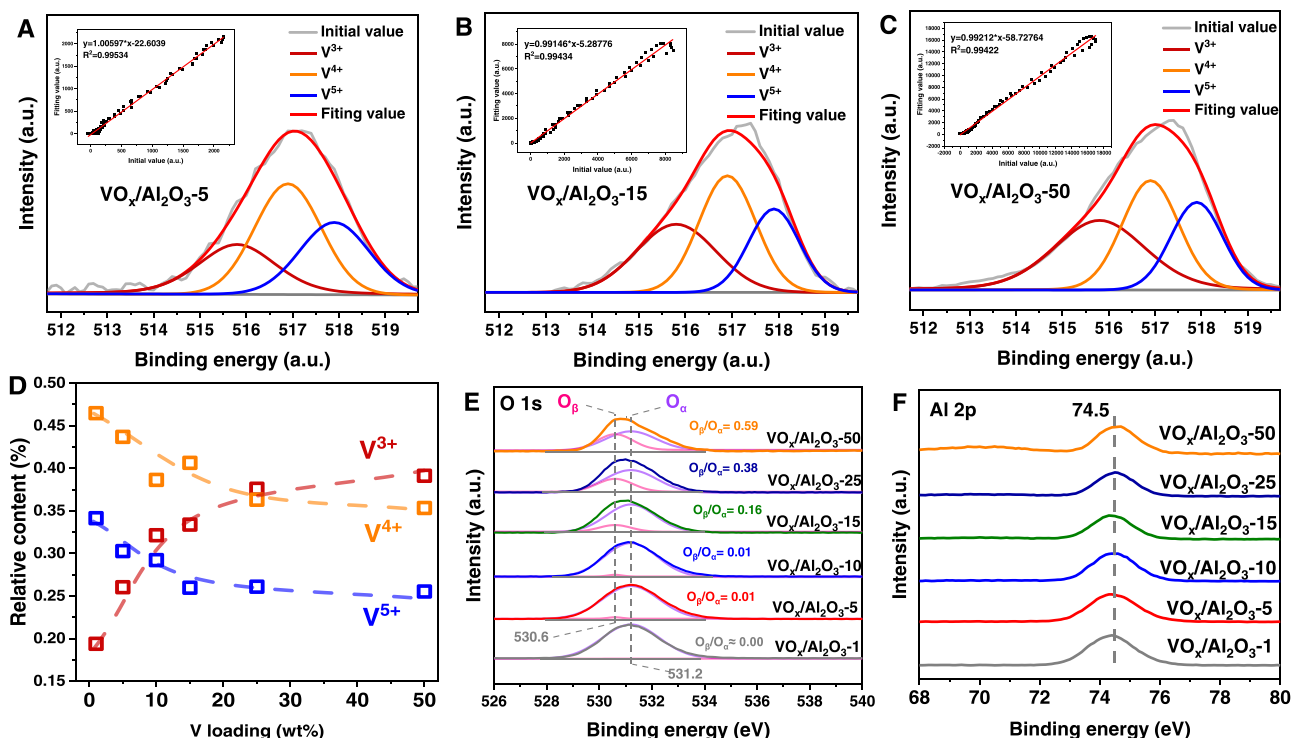


Fig. 5. XPS analysis of $\text{VO}_x/\text{Al}_2\text{O}_3$ catalysts: Peak deconvolution of V $2p_{3/2}$ of $\text{VO}_x/\text{Al}_2\text{O}_3$ -5 catalyst (A), $\text{VO}_x/\text{Al}_2\text{O}_3$ -15 catalyst (B), and $\text{VO}_x/\text{Al}_2\text{O}_3$ -50 (C). The distribution of V^{k+} valance as a function of VO_x loading amounts. (D) O 1s (E) and Al 2p (F) spectra.

attributed to the overlap of the O_α and O_β peaks. With the increase of V loading amount, the $\text{O}_\alpha/\text{O}_\beta$ ratio value increases, indicating V_2O_3 nanocrystals form gradually [47,48]. In addition, the XPS pattern of Al 2p is also shown in Fig. 5F. The Al 2p binding energy of $\text{VO}_x/\text{Al}_2\text{O}_3$ catalysts is located at 74.5 eV, which indicates the type of supported VO_x species shows an inert effect on the chemical properties of $\gamma\text{-Al}_2\text{O}_3$.

The DFT calculation was conducted to reveal the electronic property of VO_x at the atomic level. As shown in Figs. S14(A, B, and C), the isolated VO_3 , polymeric VO_3 supported on the (110) facet of $\gamma\text{-Al}_2\text{O}_3$, and the (0001) facet of crystalline V_2O_3 were constructed. The structure optimization, Bader charge analysis, and charge difference distributions of these VO_3 sites are employed by DFT calculation. As shown in Figs. S15(A, B, and C), the isolated VO_3 structure is unstable and prefers to form two additional V-O-Al bonds with $\gamma\text{-Al}_2\text{O}_3$. The charge of V^{k+} ions in isolated VO_x is -2.12 eV, indicating a highly oxidized state. For

polymeric VO_3 , one side vanadium monomer prefers to form additional V-O-Al bonds with $\gamma\text{-Al}_2\text{O}_3$, while the other side of the vanadium monomer retains its original VO_3 structure after structure optimization. The two V^{k+} ions in polymeric VO_x show a higher charge than that in isolated VO_x , which is -1.95 eV and -2.10 eV, respectively. It is consistent with the in-situ Raman and $\text{H}_2\text{-TPR}$ result. The Al_2O_3 confines the isolated VO_x in the lattice through V-O-Al bonds, while V-O-V bonds in polymeric VO_x can weaken this interaction and promote the reduction of VO_x . VO_3 structure in bulk V_2O_3 is stable after structure optimization. The charge of V^{k+} ions in V_2O_3 are -1.28 or -1.36 eV, which is much higher than V^{k+} ions in polymeric VO_x . In addition, the charge of O^{2-} ions in V_2O_3 is $+1.29$ or $+1.30$ eV, much higher than that in polymeric VO_x and isolated VO_x . Thus, the electronic property of VO_x is highly dependent on its structure, and V_2O_3 shows a higher fraction of V^{3+} ions and electronic density in O^{2-} ions than isolated and polymeric VO_x .

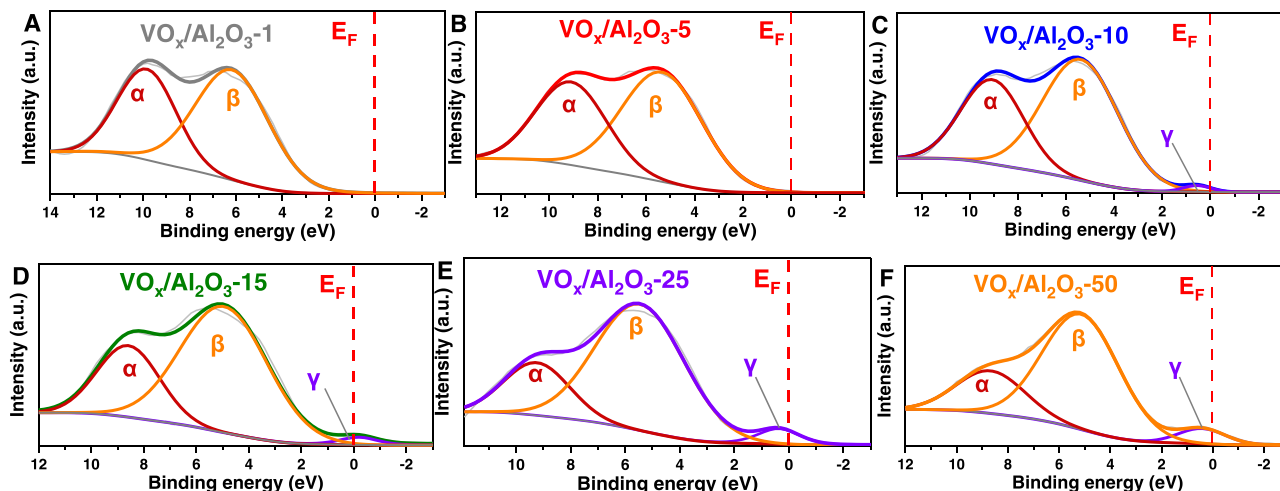


Fig. 6. XPS-VBS of $\text{VO}_x/\text{Al}_2\text{O}_3$ catalysts. (A) $\text{VO}_x/\text{Al}_2\text{O}_3$ -1; (B) $\text{VO}_x/\text{Al}_2\text{O}_3$ -5; (C) $\text{VO}_x/\text{Al}_2\text{O}_3$ -10; (D) $\text{VO}_x/\text{Al}_2\text{O}_3$ -15; (E) $\text{VO}_x/\text{Al}_2\text{O}_3$ -25; (F) $\text{VO}_x/\text{Al}_2\text{O}_3$ -50.

It is well known that electronic property has a great influence on the band structure. Thus, XPS-VBS of the as-obtained samples is conducted to investigate the band structure and Fermi level (E_F) location of $\text{VO}_x/\text{Al}_2\text{O}_3$ catalysts. As shown in Fig. 6(A, B, and C), mono-layer $\text{VO}_x/\text{Al}_2\text{O}_3$ catalysts display typically characteristic of O 2p band of Al_2O_3 and mono-layer oxide, which contains the band at around 6.0 eV (band β) and 10.0 eV (band α) [49]. There are almost no energy state levels of distribution around the position of the E_F level. As shown in Table S4, the ratio of band α to band β is also similar in all mono-layer $\text{VO}_x/\text{Al}_2\text{O}_3$ catalysts, which can fit well with the characteristic peaks of mono-layer oxide. As shown in Fig. 6(D, E, and F), the VBS of V_2O_5 -abundant catalysts shows two bands from 2.0 eV to 0 eV (band γ) and 10–2.0 eV (band α and band β), which can be attributed to V 3d band of V_2O_3 and overlapping O 2p band of V_2O_3 and Al_2O_3 , respectively [50]. Noteworthy, the V 3d band is distributed around the E_F for V_2O_5 -abundant catalysts, indicating that V_2O_3 has stronger metallic properties than isolated and polymeric VO_x . As the V_2O_5 is a semiconductor, the abnormal metallicity of the V_2O_5 -abundant catalyst can be attributed to the special electronic and geometric property of in-situ formed V_2O_3 after reduction. The V^{3+} ions are in unstable intermediate valence between metallic V^0 and oxidized V^{5+} ions. To achieve a stable electronic state, the high fraction of V^{3+} ions in the V_2O_3 can promote V 3d electron delocalization and transfer to adjoining V^{3+} ions. In addition, the 3D structure of V_2O_3 exhibits an advantage in electron transfer compared to the 2D structure of polymeric VO_x . Thus, V 3d electrons in V_2O_3 can spontaneously transfer through $\text{V}^{3+}\text{-O-V}^{3+}$ bonds. In addition, the intensity of band β and band γ increase with increased V loading amount, which confirm the gradually formed V_2O_3 nanocrystals on V_2O_5 -abundant $\text{VO}_x/\text{Al}_2\text{O}_3$ catalysts with increasing V loading amount.

The UV–VIS–NIR spectra were conducted to investigate the light absorption capacity of $\text{VO}_x/\text{Al}_2\text{O}_3$ catalysts. To reveal the role of propane, the light adsorption of both fresh and reduced $\text{VO}_x/\text{Al}_2\text{O}_3$ catalysts is shown in Fig. 7(A and B). After propane treatment, $\text{VO}_x/\text{Al}_2\text{O}_3$ -1 catalyst exhibits a new adsorbed band centered at 600 nm in the range of 400–1200 nm. For $\text{VO}_x/\text{Al}_2\text{O}_3$ -10 catalyst, the range of this new adsorbed band broadens to 1600 nm, and the adsorption efficiency increases compared to that of $\text{VO}_x/\text{Al}_2\text{O}_3$ -1 catalyst, indicating that the new adsorbed band is closely related to the structure of VO_x . As shown in Fig. 7C, propane treatment hardly changes the structure of isolated and polymeric VO_x but breaks the V=O bonds. During this process, the charge transfers from the removed V=O bonds to center V^{5+} ions as

neutral charge, which occupies the originally empty V 3d orbit and generates reduced V^{4+} ions ($\& = 3, 4$). The V^{4+} and V^{3+} ions have $3d^1$ and $3d^2$ electron states, respectively. The VIS light can excite V 3d electrons to the high level of d orbital, which is defined as d-d transition. The decreased band in the UV region results from the consumption of V^{5+} ions [51]. Compared to isolated VO_x , the V-O-V bonds in polymeric VO_x can promote the break of V=O bonds and the formation of V^{3+} ions with additive V 3d electrons, which is beneficial to enhance the d-d transition. Thus, the improved VIS light adsorption in $\text{VO}_x/\text{Al}_2\text{O}_3$ -10 catalyst is attributed to additional V^{3+} ions in polymeric VO_x .

As shown in Fig. 7(D and E), the optical property of V_2O_5 -abundant catalysts is further improved compared to monolayer catalysts. After exposure to propane, the $\text{VO}_x/\text{Al}_2\text{O}_3$ -15 catalyst shows stronger adsorption for VIS and NIR light region than the $\text{VO}_x/\text{Al}_2\text{O}_3$ -10 catalyst, in which the adsorbed band centered at 1000 nm in the range of 400–2000 nm appears. $\text{VO}_x/\text{Al}_2\text{O}_3$ -50 catalyst displays strong light absorption across the full spectrum, and its response in VIS and NIR region is much stronger than $\text{VO}_x/\text{Al}_2\text{O}_3$ -15 catalyst. As shown in Fig. 7F, the polymeric VO_x of the used $\text{VO}_x/\text{Al}_2\text{O}_3$ -15 catalyst is transformed to V_2O_3 , while V_2O_3 is dominated by the reduced $\text{VO}_x/\text{Al}_2\text{O}_3$ -50 catalyst. Compared to mono-layer VO_x , the increased V^{3+} sites in V_2O_3 are beneficial for improving the d-d transition and the adsorption for visible light. However, the new adsorbed band of the V_2O_5 -abundant catalyst is much higher and broader than the adsorbed band of the d-d transition. Based on the VBS, the metallic nature of V_2O_3 also plays an important role in improving the optical property. The fluctuation of electron-induced by irradiation would cause the collective vibration of the whole electronic system in conductive material through coulomb force, and resonance of these electrons can significantly increase light adsorption in VIS or NIR region, which is called localized surface plasmonic resonance (LSPR) [52]. Except for typically plasmonic metals, such as Au, and Ag, the LSPR can also present in oxide with a low chemical state and strong metallicities, such as BiO_2 , and WO_2 [53]. The VBS of V_2O_5 -abundant catalysts exhibits an overlapping E_F and V 3d band, inferring a strong metallicity of V_2O_3 . The high fraction of V^{3+} ions in V_2O_3 nanocrystals can benefit to excite the fluctuation of the electrons, and its 3D structure improves the coupling of electromagnetic waves between $\text{V}^{3+}\text{-O-V}^{3+}$ bonds. Thus, the increased VIS and NIR light adsorption efficiency is assigned to the LSPR effect of V_2O_3 , which is dismissed in isolated and polymeric VO_x due to their poor plasmonic property. In addition, the increased IR adsorption at > 2000 nm is

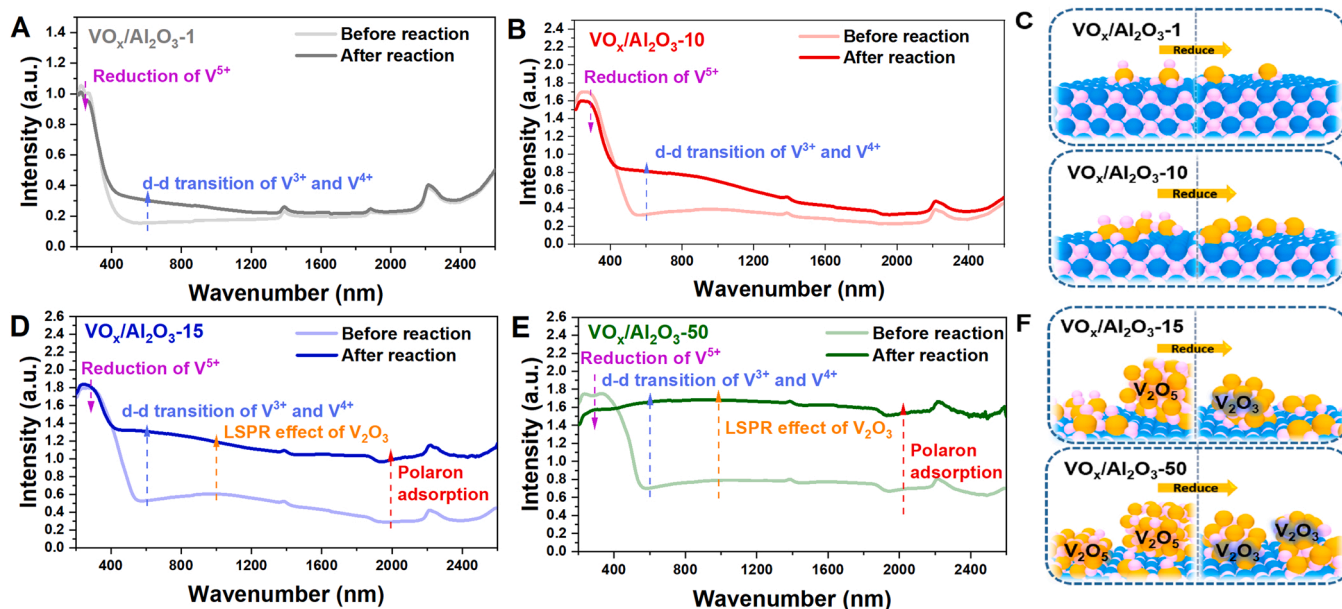


Fig. 7. UV–VIS–NIR spectra of $\text{VO}_x/\text{Al}_2\text{O}_3$ catalysts and corresponding structure transformation (A–F). (Orange, V atoms; Pink, O atoms; Blue, Al atoms).

attributed to the phonon vibration and polaron absorption in the 3D lattice of V_2O_3 nanocrystals [54,55]. To disclose the role of light adsorption, the absorption efficiency for the six VO_x/Al_2O_3 catalysts and bulk V_2O_3 at varied wavelengths are shown in Fig. S16. For VO_x/Al_2O_3 catalysts, the adsorption in the VIS and NIR light region gradually increases with increasing VO_x loading amount, while there is barely any change in UV light (320 nm) adsorption for V_2O_5 -abundant VO_x/Al_2O_3 catalysts. The V_2O_5 -abundant VO_x/Al_2O_3 catalysts show much higher light adsorption efficiency in 550, 780, and 1000 nm than mono-layer VO_x/Al_2O_3 catalysts. During the PDH test, the wavelength of the light source is 320–780 nm. The range of increasing adsorption efficiency shows a good correlation with the rising photothermal activity (D value), indicating that the high photothermal activity of the V_2O_5 -abundant catalyst is attributed to the strong light adsorption of the V_2O_3 component.

Based on these results, the structure-dependent optical properties of VO_x during photothermal PDH reaction can be revealed. The V^{3+} ions with a $3d^2$ shell are more active in the d-d transition than V^{4+} ions, which leads to improved light absorption efficiency for VIS and NIR. The $V^{3+}-O-V^{3+}$ bonds in V_2O_3 nanocrystals can lead to strong resonance absorption for VIS and NIR regions induced by the LSPR effect [56]. After the treatment of propane, the V-based material is earth-abundant and exhibits strong light adsorption in the full spectrum. The

understanding of structure-depending optical properties of VO_x provides an affordable and controllable way to develop a high-effective photothermal catalyst.

3.5. Catalytic mechanism of VO_x/Al_2O_3 catalysis

According to UV–VIS–NIR spectra, the light absorption efficiency of the VO_x/Al_2O_3 catalyst is well correlated with its photothermal PDH activity. In general, irradiation can participate in reaction through three paths: The changing structural and electronic properties of materials; The motivating electron-hole pairs; And the producing additional heat (or called photothermal effect) [57]. To explore the promoting mechanism of irradiation, the effects of several kinetic factors in the reaction were tested. As shown in Fig. 8A, the space speed of the VO_x/Al_2O_3 -15 catalyst was adjusted to reach its equilibrium conversion. The propane conversion keeps unchanged as the WHSV lower than 0.12 h^{-1} , indicating that reaches the reaction thermodynamic equilibrium of PDH. If the promoting role of irradiation is mainly caused by the light-induced structural or electronic change, it is predictable that the propane conversion under irradiation should not exceed the value in thermodynamic limitation. However, the activity of the VO_x/Al_2O_3 -15 catalyst significantly improves and exceeds the equilibrium conversion rate under irradiation, which indicates the thermodynamic equilibrium of PDH is

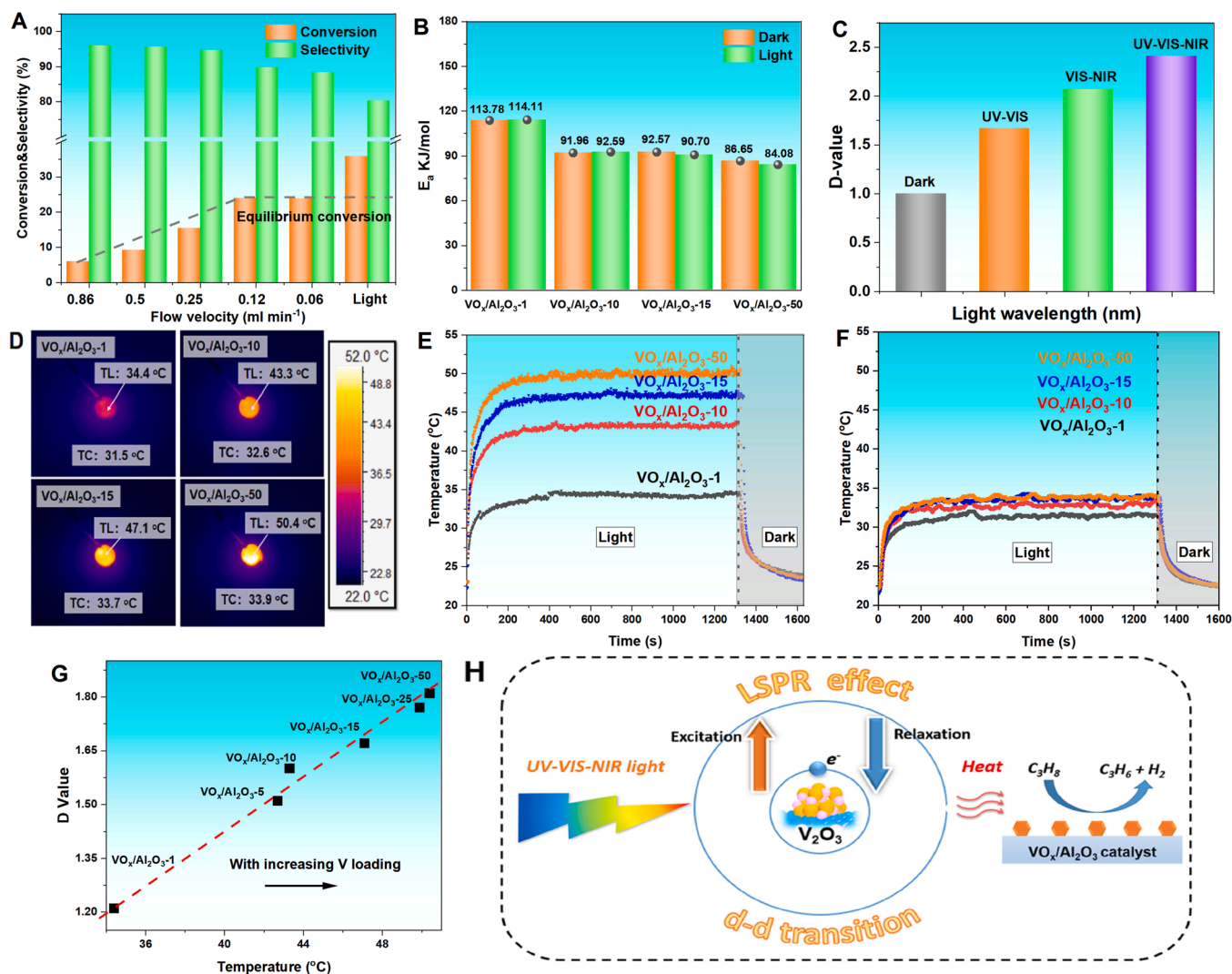


Fig. 8. The propane conversion of VO_x/Al_2O_3 -15 catalyst at different space speeds (A), activation energy of VO_x/Al_2O_3 catalysts under dark and irradiation (B), D value of VO_x/Al_2O_3 -15 catalyst as a function of wavelength (C), IR camera image (D), local temperature (E), catalyst temperature (F), the relationship between D value and local temperature (F), and reaction mechanism diagram (H) of VO_x/Al_2O_3 catalysts. (Orange, V atoms; Pink, O atoms; Blue, Al atoms).

changed by illumination.

To further reveal the catalytic mechanism, as shown in Fig. S17, the apparent activation energy (E_a) of $\text{VO}_x/\text{Al}_2\text{O}_3$ catalysts under irradiation and dark was calculated through the Arrhenius equation. As shown in Fig. 8B, $\text{VO}_x/\text{Al}_2\text{O}_3$ -1 catalyst possesses the highest E_a , (113.78 kJ/mol), while the E_a value of $\text{VO}_x/\text{Al}_2\text{O}_3$ -10 and $\text{VO}_x/\text{Al}_2\text{O}_3$ -15 catalysts is 91.96 and 92.57 kJ/mol, respectively. The E_a value of the $\text{VO}_x/\text{Al}_2\text{O}_3$ -50 catalyst is the lowest, which is 86.65 kJ/mol. In general, photogenerated electrons can participate in some reaction paths or change the electron structure of active sites for facilitating reaction pathways, this promotion mechanism can lead to a change in the activation energy (E_a) of the reaction. Under irradiation, the E_a values of all catalysts are barely changed, indicating the incident light cannot change the elementary reaction steps of the PDH reaction. Therefore, the photogenerated electron-hole pairs would not be directly involved in the cleaver of the C-H bonds on $\text{VO}_x/\text{Al}_2\text{O}_3$ catalysts during the photothermal PDH process. In addition, the catalytic process with the photogenerated electron mechanism always shows the dependence of the activity on the wavelength of light. In the contrast, the catalytic process with a photothermal effect is only related to the adsorption of irradiation flux but is less dependent on the wavelength of light [58]. As shown in Fig. 8C, the catalytic activities of $\text{VO}_x/\text{Al}_2\text{O}_3$ -15 catalyst under different wavelengths of light were tested. $\text{VO}_x/\text{Al}_2\text{O}_3$ -15 catalyst obtain the highest activity under full-spectrum light irradiation, while activity decreases after the removal of UV or NIR light. The light with different wavelengths all contributes to activity, which is the typical characteristic of the photothermal effect. Thus, the photothermal effect is the main reason for promoting the activity of catalysts.

As the enhanced catalytic activity is from the photothermal effect, the local temperature (TL) of the catalyst surface is essential. The in-situ IR camera was conducted to detect the TL of $\text{VO}_x/\text{Al}_2\text{O}_3$ catalysts under irradiation. As shown in Fig. 8D and S18(A, B), the TL of $\text{VO}_x/\text{Al}_2\text{O}_3$ catalysts is higher than room temperature (22.6 °C), indicating that the VO_x component can increase surface temperature through the photothermal effect. The TL is closely related to the light adsorption of catalysts. $\text{VO}_x/\text{Al}_2\text{O}_3$ -1 catalyst shows the lowest TL (34.4 °C). For $\text{VO}_x/\text{Al}_2\text{O}_3$ -10 catalyst, its TL is 43.3 °C, which can be attributed to the higher light adsorption of polymeric VO_x than isolated VO_x . As the adsorption efficiency of V_2O_3 is higher than isolated and polymeric VO_x , V_2O_5 -abundant catalysts show a much higher TL than mono-layer catalysts. The $\text{VO}_x/\text{Al}_2\text{O}_3$ -50 catalyst, which consists mainly of V_2O_3 nanocrystals, exhibits the highest TL (50.4 °C). The TL rise curve is shown in Fig. 8E. The surface of $\text{VO}_x/\text{Al}_2\text{O}_3$ catalysts is heated up immediately under irradiation and rapidly cooled down to room temperature once removed from irradiation. In addition, the temperature of the catalyst bulk (TC) is tested by the thermocouple, which is buried within the catalyst. As shown in Fig. 8F, the TC only slightly increases after irradiation, indicating that irradiation selectively heats VO_x active sites on the catalyst surface without affecting the temperature of catalyst bulk. Compared with the traditional heating method, this photothermal method can reduce energy use [59]. To confirm that the local temperature was responsible for the enhancement of PDH activity, Fig. 8G exhibits the plot of the photothermal efficiency (D-value) as a function of the TL. There is a positive linear correlation between the photothermal efficiency and the surface temperature of the catalyst. Therefore, the catalytic mechanism under irradiation can be determined as the photothermal effect of the VO_x component.

In summary, the photothermal catalytic mechanism of the $\text{VO}_x/\text{Al}_2\text{O}_3$ catalyst can be determined. As illustrated in Fig. 8H, the supported VO_x component acts as both photocatalytic and thermocatalytic active sites. The 3D V_2O_3 nanocrystal exhibits strong light absorption in the full spectrum, which is attributed to its d-d transition and LSPR effect. Under irradiation, the excitation and relaxation of electrons in V^{3+} ions produce additional heat, which promotes the cleavage of C-H bonds.

4. Conclusions

A series of $\text{VO}_x/\text{Al}_2\text{O}_3$ catalysts with a controllable surface state of VO_x were successfully synthesized by the impregnation method. The PDH catalytic activity of the $\text{VO}_x/\text{Al}_2\text{O}_3$ catalyst can be remarkably enhanced under UV-VIS light irradiation. Among the $\text{VO}_x/\text{Al}_2\text{O}_3$ catalysts, $\text{VO}_x/\text{Al}_2\text{O}_3$ -25 catalyst shows the excellent performance for photothermal catalytic PDH, i.e., its propane conversion rate is 20.7 % at 480 °C, and its K_d value is only 0.018 h⁻¹. The actual structure and optical properties of VO_x are revealed by in-situ XRD, in-situ UV-Raman, DFT calculation, and UV-VIS-NIR. The propane treatment can break the V=O bonds of VO_x to produce light-active V^{3+} ions, which adsorb VIS light through the d-d transition. V-O-V bonds on polymeric VO_x can promote the formation of more active V^{3+} ions compared to isolated VO_x . For V_2O_5 -abundant catalysts, the V_2O_5 can be dispersed into polymeric VO_x , which further reconstructs to 3D V_2O_3 nanocrystals during the PDH reaction. The unique 3D V^{3+} -O- V^{3+} unit in V_2O_3 shows strong light adsorption in the full spectrum, which is attributed to the d-d transition and LSPR effect. The improved light adsorption efficiency can provide additional heat, thus accelerating PDH activity. Insight into the structural-dependent property of VO_x and V-based catalysts for photothermal PDH is expected to obtain high-efficient and environmental catalysts in practical application.

CRedit authorship contribution statement

Bohan Feng: Conceptualization, Data curation, Formal analysis, Investigation, Methodology, Writing – original draft, **Dong Li:** Data curation, Formal analysis, Investigation, **Jing Xiong:** Writing – review & editing, Supporting, **Yuechang Wei:** Project administration, Supervision, Validation, Writing – review & editing, **Yuanfeng Li:** Investigation, **Zhen Zhao:** Project administration, Validation, Weiyu Song: Funding acquisition, Project administration, Software, **Xiangyang Ji:** Investigation, Jian Liu: Funding acquisition, Project administration, Validation, **Chunming Xu:** Project administration, Validation, Writing – review & editing.

Declaration of Interest

The authors declare that they have no known competing financial interests or personal relationships that could have appeared to influence the work reported in this paper.

Data Availability

Date not available to be shared.

Acknowledgment

This work was supported by the National Natural Science Foundation of China (21972166, 22035009), Beijing Natural Science Foundation (2202045), the National Key Research and Development Program of China (2019YFC1907600, 2021YFA1501300) and the Science Foundation of China University of Petroleum, Beijing (2462021YJRC018).

Appendix A. Supporting information

Supplementary data associated with this article can be found in the online version at [doi:10.1016/j.apcatb.2022.122337](https://doi.org/10.1016/j.apcatb.2022.122337).

References

- [1] J.J.H.B. Sattler, J. Ruiz-Martinez, E. Santillan-Jimenez, B.M. Weckhuysen, Catalytic dehydrogenation of light alkanes on metals and metal oxides, *Chem. Rev.* 114 (2014) 10613–10653.

- [2] S. Lawson, K. Baamran, K. Newport, T. Alghamadi, G. Jacobs, F. Rezaei, A. A. Rowanghi, Integrated direct air capture and oxidative dehydrogenation of propane with CO₂ at isothermal conditions, *Appl. Catal. B* 303 (2022), 120907.
- [3] Y. Gu, H. Liu, M. Yang, Z. Ma, L. Zhao, W. Xing, P. Wu, X. Liu, S. Mintova, P. Bai, Z. Yan, Highly stable phosphine modified VO_x/Al₂O₃ catalyst in propane dehydrogenation, *Appl. Catal. B* 274 (2020), 119089.
- [4] Y. Liu, L. Luo, Y. Gao, W. Huang, CeO₂ morphology-dependent NbO_x-CeO₂ interaction, structure and catalytic performance of NbO_x/CeO₂ catalysts in oxidative dehydrogenation of propane, *Appl. Catal. B* 197 (2016) 214–221.
- [5] G. Sun, Z. Zhao, R. Mu, S. Zha, L. Li, S. Chen, K. Zang, J. Luo, Z. Li, S.C. Purdy, A. J. Kropf, J.T. Miller, L. Zeng, J. Gong, Breaking the Scaling Relationship Via Thermally Stable Pt/Cu Single Atom Alloys for Catalytic Dehydrogenation, *Nat. Commun.* 9 (2018).
- [6] R. Ryoo, J. Kim, C. Jo, S.W. Han, J. Kim, H. Park, J. Han, H.S. Shin, J.W. Shin, Rare-earth-platinum alloy nanoparticles in mesoporous zeolite for catalysis, *Nature* 585 (2020) 221–224.
- [7] J. Wang, Y. Song, Z. Liu, Z. Liu, Active and selective nature of supported CrO_x for the oxidative dehydrogenation of propane with carbon dioxide, *Appl. Catal. B* 297 (2021), 120400.
- [8] Y. Zhang, Y. Zhao, T. Otroshchenko, H. Lund, M. Pohl, U. Rodemerck, D. Linke, H. Jiao, G. Jiang, E.V. Kondratenko, Control of coordinatively unsaturated Zr sites in ZrO₂ for efficient C–H bond activation, *Nat. Commun.* 9 (2018).
- [9] P. Wang, J. Yao, Q. Jiang, X. Gao, D. Lin, H. Yang, L. Wu, Y. Tang, L. Tan, Stabilizing the isolated Pt sites on PtGa/Al₂O₃ catalyst via silica coating layers for propane dehydrogenation at low temperature, *Appl. Catal. B* 300 (2022), 120731.
- [10] Z. Zhao, T. Wu, C. Xiong, G. Sun, R. Mu, L. Zeng, J. Gong, Hydroxyl-mediated non-oxidative propane dehydrogenation over VO_x/γ-Al₂O₃ catalysts with improved stability, *Angew. Chem. Int. Ed.* 57 (2018) 6791–6795.
- [11] W. Wei, Z. Wei, R. Li, Z. Li, R. Shi, S. Ouyang, Y. Qi, D.L. Philips, H. Yuan, Subsurface oxygen defects electronically interacting with active sites on In₂O₃ for enhanced photothermocatalytic CO₂ reduction, *Nat. Commun.* 13 (2022).
- [12] Y. Qi, J. Jiang, X. Liang, S. Ouyang, W. Mi, S. Ning, L. Zhao, J. Ye, Fabrication of black In₂O₃ with dense oxygen vacancy through dual functional carbon doping for enhancing photothermal CO₂ hydrogenation, *Adv. Funct. Mater.* 31 (2021), 2100908.
- [13] S. Luo, H. Lin, Q. Wang, X. Ren, D. Hernández-Pinilla, T. Nagao, Y. Xie, G. Yang, S. Li, H. Song, M. Oshikiri, J. Ye, Triggering water and methanol activation for solar-driven H₂ production: interplay of dual active sites over plasmonic ZnCu alloy, *J. Am. Chem. Soc.* 143 (2021) 12145–12153.
- [14] Z. Liu, L. Niu, X. Zong, L. An, D. Qu, X. Wang, Z. Sun, Ambient photothermal catalytic CO oxidation over a carbon-supported palladium catalyst, *Appl. Catal. B* 313 (2022), 121439.
- [15] M.A. Nadeem, H. Idriss, Effect of temperature on the photoreactions of ethanol over Ag/TiO₂ in steady state catalytic conditions, *Appl. Catal. B* 284 (2021), 119736.
- [16] D. Nozik, F.M.P. Tinga, A.T. Bell, Propane dehydrogenation and cracking over Zn/H-MFI prepared by solid-state ion exchange of ZnCl₂, *ACS Catal.* (2021) 14489–14506.
- [17] G. Liu, Z. Zhao, T. Wu, L. Zeng, J. Gong, Nature of the active sites of VO_x/Al₂O₃ catalysts for propane dehydrogenation, *ACS Catal.* (2016) 5207–5214.
- [18] D.E. Keller, S.M.K. Airaksinen, A.O. Krause, B.M. Weckhuysen, D.C. Koningsberger, Atomic XAFS as a tool to probe the reactivity of metal oxide catalysts: quantifying metal oxide support effects, *J. Am. Chem. Soc.* 129 (2007) 3189–3197.
- [19] P. Bai, Z. Ma, T. Li, Y. Tian, Z. Zhang, Z. Zhong, W. Xing, P. Wu, X. Liu, Z. Yan, Relationship between surface chemistry and catalytic performance of mesoporous γ-Al₂O₃ supported VO_x catalyst in catalytic dehydrogenation of propane, *ACS Appl. Mater. Inter.* 8 (2016) 25979–25990.
- [20] Y. Xie, R. Luo, G. Sun, S. Chen, Z. Zhao, R. Mu, J. Gong, Facilitating the Reduction of V–O Bonds on VO_x/ZrO₂ catalysts for non-oxidative propane dehydrogenation, *Chem. Sci.* 11 (2020) 3845–3851.
- [21] P. Hu, Y. Chen, X. Yan, W. Lang, Y. Guo, Correlation of the vanadium precursor and structure performance of porous VO_x-SiO₂ solids for catalytic dehydrogenation of propane, *Ind. Eng. Chem. Res.* 58 (2019) 4065–4073.
- [22] U. Rodemerck, M. Stoyanova, E.V. Kondratenko, D. Linke, Influence of the kind of VO_x structures in VO_x/MCM-41 on activity, selectivity and stability in dehydrogenation of propane and isobutane, *J. Catal.* 352 (2017) 256–263.
- [23] S. Sokolov, M. Stoyanova, U. Rodemerck, D. Linke, E.V. Kondratenko, Comparative study of propane dehydrogenation Over V-, Cr-, and Pt-based catalysts: time on-stream behavior and origins of deactivation, *J. Catal.* 293 (2012) 67–75.
- [24] J. Scholz, A. Walter, T. Ressler, Influence of MgO-modified SBA-15 on the structure and catalytic activity of supported vanadium oxide catalysts, *J. Catal.* 309 (2014) 105–114.
- [25] X. Fan, D. Liu, X. Sun, X. Yu, D. Li, Y. Yang, H. Liu, J. Diao, Z. Xie, L. Kong, X. Xiao, Z. Zhao, Mn-doping induced changes in Pt dispersion and Pt₃Mn₂ alloying extent on Pt/Mn-DMSN catalyst with enhanced propane dehydrogenation stability, *J. Catal.* 389 (2020) 450–460.
- [26] Y. Inomata, H. Kubota, S. Hata, E. Kiyonaga, K. Morita, K. Yoshida, N. Sakaguchi, T. Toyao, K. Shimizu, S. Ishikawa, W. Ueda, M. Haruta, T. Murayama, Bulk tungsten-substituted vanadium oxide for low-temperature NO_x removal in the presence of water, *Nat. Commun.* 12 (2021).
- [27] A. Cao, J. Hu, H. Liang, L. Wan, Self-assembled vanadium pentoxide (V₂O₅) hollow microspheres from nanorods and their application in lithium-ion batteries, *Angew. Chem. Int. Ed.* 44 (2005) 4391–4395.
- [28] S. Chen, C. Pei, X. Chang, Z.J. Zhao, R. Mu, Y. Xu, J. Gong, Coverage-dependent behaviors of vanadium oxides for chemical looping oxidative dehydrogenation, *Angew. Chem. Int. Ed.* 59 (2020) 22072–22079.
- [29] R. Baddour-Hadjean, J.P. Pereira-Ramos, C. Navone, M. Smirnov, Raman microspectrometry study of electrochemical lithium intercalation into sputtered crystalline V₂O₅ thin films, *Chem. Mater.* 20 (2008) 1916–1923.
- [30] Z. Wu, H. Kim, P.C. Stair, S. Rugmini, S.D. Jackson, On the structure of vanadium oxide supported on aluminas: UV and visible raman spectroscopy, UV–visible diffuse reflectance spectroscopy, and temperature-programmed reduction studies, *J. Phys. Chem. B* 109 (2005) 2793–2800.
- [31] X. Gao, S.R. Bare, B.M. Weckhuysen, I.E. Wachs, In situ spectroscopic investigation of molecular structures of highly dispersed vanadium oxide on silica under various conditions, *J. Phys. Chem. B* 102 (1998) 10842–10852.
- [32] J. Yan, A. Rath, H. Wang, Z.Q.C. Ng, S.J. Pennycook, D.H.C. Chua, Tungsten suboxide nanoneedles as an effective thermal shield through near-infrared reflection and absorption, *J. Phys. Chem. C* 125 (2021) 11115–11123.
- [33] X. Gao, I.E. Wachs, Investigation of surface structures of supported vanadium oxide catalysts by UV–vis–NIR diffuse reflectance spectroscopy, *J. Phys. Chem. B* 104 (6) (2000) 1261–1268.
- [34] L.G. Cesar, C. Yang, Z. Lu, Y. Ren, G. Zhang, J.T. Miller, Identification of a Pt₃Co surface intermetallic alloy in Pt-Co propane dehydrogenation catalysts, *ACS Catal.* 9 (2019) 5231–5244.
- [35] X. Liu, C. Xing, F. Yang, Z. Liu, Y. Wang, T. Dong, L. Zhao, H. Liu, W. Zhou, Strong Interaction over ru/defects-rich aluminium oxide boosts photothermal CO₂ methanation via microchannel flow-type system, *Adv. Energy Mater.* 12 (2022), 2201009.
- [36] J. Zhang, Y. Li, J. Sun, H. Chen, Y. Zhu, X. Zhao, L. Zhang, S. Wang, H. Zhang, X. Duan, L. Shi, S. Zhang, P. Zhang, G. Shao, M. Wu, S. Wang, H. Sun, Regulation of energetic hot carriers on Pt/TiO₂ with thermal energy for photothermal catalysis, *Appl. Catal. B* 309 (2022), 121263.
- [37] X. Zhang, C. Xu, L. Zhang, Z. Li, J. Hong, Y. Zhang, Photothermal catalytic water splitting at diverse two-phase interfaces based on Cu–TiO₂, *ACS Appl. Energy Mater.* 5 (2022) 4564–4576.
- [38] Z. Lian, S. Ali, T. Liu, C. Si, B. Li, D.S. Su, Revealing the janus character of the coke precursor in the propane direct dehydrogenation on Pt catalysts from a kMC simulation, *ACS Catal.* 8 (2018) 4694–4704.
- [39] Z. Lian, J. Wei, W. Shan, Y. Yu, P.M. Radjenovic, H. Zhang, G. He, F. Liu, J. Li, Z. Tian, H. He, Adsorption-induced active vanadium species facilitate excellent performance in low-temperature catalytic NO_x abatement, *J. Am. Chem. Soc.* 143 (2021) 10454–10461.
- [40] L. Zhang, Y. Liu, Z. Zhao, P. Jiang, T. Zhang, M. Li, S. Pan, T. Tang, T. Wu, P. Liu, Y. Hou, H. Lu, Enhanced polysulfide regulation via porous catalytic V₂O₅/V₈C₇ heterostructures derived from metal-organic frameworks toward high-performance Li-S batteries, *ACS Nano* 14 (2020) 8495–8507.
- [41] J. Jehng, G. Deo, B.M. Weckhuysen, I.E. Wachs, Effect of water vapor on the molecular structures of supported vanadium oxide catalysts at elevated temperatures, *J. Mol. Catal. A-Chem.* 110 (1996) 41–54.
- [42] J.Z. Hu, S. Xu, W. Li, M.Y. Hu, X. Deng, D.A. Dixon, M. Vasiliu, R. Craciun, Y. Wang, X. Bao, C.H.F. Peden, Investigation of the structure and active sites of TiO₂ nanorod supported VO_x catalysts by high-field and fast-spinning ⁵¹V MAS NMR, *ACS Catal.* 5 (2015) 3945–3952.
- [43] Z. Wu, P.C. Stair, S. Rugmini, S.D. Jackson, Raman spectroscopic study of V/θ-Al₂O₃ catalysts: quantification of surface vanadia species and their structure reduced by hydrogen, *J. Phys. Chem. C* 111 (2007) 16460–16469.
- [44] N. Sa, T.L. Kinnibrugh, H. Wang, G. Sai Gautam, K.W. Chapman, J.T. Vaughey, B. Key, T.T. Fister, J.W. Freeland, D.L. Proffitt, P.J. Chupas, G. Ceder, J.G. Baren, I. D. Bloom, A.K. Burrell, Structural evolution of reversible mg insertion into a bilayer structure of V₂O₅ nH₂O xerogel material, *Chem. Mater.* 28 (2016) 2962–2969.
- [45] J. Yu, Y. Yu, P. Zhou, W. Xiao, B. Cheng, Morphology-dependent photocatalytic H₂-production activity of CdS, *Appl. Catal. B* 156–157 (2014) 184–191.
- [46] Z. Zhao, T. Wu, C. Xiong, et al., Hydroxyl-mediated non-oxidative propane dehydrogenation over VO_x/γ-Al₂O₃ catalysts with improved stability, *Angew. Chem. Int. Ed.* 57 (23) (2018) 6791–6795.
- [47] J. Choi, The surface properties of vanadium compounds by X-ray photoelectron spectroscopy, *Appl. Surf. Sci.* 148 (1999) 64–72.
- [48] H. Huang, Y. Gu, J. Zhao, X. Wang, Catalytic combustion of chlorobenzene over VO_x/CeO₂ catalysts, *J. Catal.* 326 (2015) 54–68.
- [49] R. Jung, J. Lee, Y. So, T. Noh, S.J. Oh, J. Lee, H. Shin, Bandgap states in transition-metal (Sc, Y, Zr, and Nb)-doped Al₂O₃, *Appl. Phys. Lett.* 83 (2003) 5226–5228.
- [50] S.S. Majid, D.K. Shukla, F. Rahman, K. Gautam, R.J. Choudhary, V.G. Sathe, D. M. Phase, Stabilization of metallic phase in V₂O₃ thin film, *Appl. Phys. Lett.* 110 (2017), 173101.
- [51] X. Gao, J. Jehng, I.E. Wachs, In Situ UV–Vis–NIR diffuse reflectance and raman spectroscopic studies of propane oxidation over ZrO₂-supported vanadium oxide catalysts, *J. Catal.* 209 (2002) 43–50.
- [52] J. Li, S.K. Cushing, J. Bright, F. Meng, T.R. Senty, P. Zheng, A.D. Bristow, N. Wu, Ag@Cu₂O core-shell nanoparticles as visible-light plasmonic photocatalysts, *ACS Catal.* 3 (2013) 47–51.
- [53] X. Liu, L. Yang, M. Huang, Q. Li, L. Zhao, Y. Sang, X. Zhang, Z. Zhao, H. Liu, W. Zhou, Oxygen vacancy-regulated metallic semiconductor MoO₂ nanobelt photoelectron and hot electron self-coupling for photocatalytic CO₂ reduction in pure water, *Appl. Catal. B* 319 (2022), 121887.
- [54] G.A. Niklasson, C.G. Granqvist, Electrochromics for smart windows: thin films of tungsten oxide and nickel oxide, and devices based on these, *J. Mater. Chem.* 17 (2) (2007) 127–156.
- [55] M.F. Saenger, T. Höing, B.W. Robertson, et al., Polaron and phonon properties in proton intercalated amorphous tungsten oxide thin films, *Phys. Rev. B* 78 (24) (2008).

- [56] Z. Lin, J. Li, Z. Zheng, J. Yan, P. Liu, C. Wang, G. Yang, Electronic reconstruction of α -Ag₂WO₄ nanorods for visible-light photocatalysis, *ACS Nano* 9 (2015) 7256–7265.
- [57] Y. Zhou, D.E. Doronkin, Z. Zhao, P.N. Plessow, J. Jelic, B. Detlefs, T. Pruessmann, F. Studt, J. Grunwaldt, Photothermal catalysis over nonplasmonic Pt/TiO₂ studied by operando HERFD-XANES, resonant XES, and DRIFTS, *ACS Catal.* 8 (2018) 11398–11406.
- [58] X. Meng, T. Wang, L. Liu, S. Ouyang, P. Li, H. Hu, T. Kako, H. Iwai, A. Tanaka, J. Ye, Photothermal conversion of CO₂ Into CH₄ with H₂ over groupVIII nanocatalysts: an alternative approach for solar fuel production, *Angew. Chem. Int. Ed.* 53 (2014) 11478–11482.
- [59] J. Ren, S. Ouyang, H. Xu, X. Meng, T. Wang, D. Wang, J. Ye, Targeting activation of CO₂ and H₂ over Ru-loaded ultrathin layered double hydroxides to achieve efficient photothermal CO₂ methanation in flow-type system, *Adv. Energy Mater.* 7 (2017), 1601657.